Background Studies and Detection of the Y_c Decay Products for P50

the P50 collaboration

18 September, 2013

1. Background simulation

Background generators

The main contribution of the background is the multi-meson production including the strangeness. For the estimation of the background, the JAM [1] code was used. The results from JAM were checked by old experimental data and compared with the PYTHIA [2] code.

The JAM code covers those three energy regions, the resonance region ($\sqrt{s} < 4$ GeV), the string region ($4 < \sqrt{s} < 10$ GeV) and the pQCD region ($\sqrt{s} > 10$ GeV). The energy region used in the proposed experiment is the string region. In this region, the string-string scattering processes mainly generate hadrons. The hadronization process is described from the Lund String model [3] which is also adopted by the PYTHIA code. The conditions of the string-string scattering and the hadronization processes are adjusted and tuned for reproducing the experimental data as following, no string-string scattering before hadronization, no color flow during the string generation, and to input the measured ratio of the generated hadron resonances in the hadronization process, such as $\frac{\rho}{\rho+\pi} = 0.5$ and $\frac{K^*}{K^*+K} = 0.6$. Those conditions and input hadron resonances are different from the PYTHIA code. Both simulation codes were checked and compared with the experimental data.

Background generator check

For comparing the old experimental data with the similar kinematical conditions, it is necessary for the clear experimental information such as detector acceptance and conditions of event selections. However, there are little available experimental data which clearly include those experimental information. Those data are few available cases to check the simulation results. For the invariant mass information by using the π^- p reaction, the BNL experiment [4] with the beam momentum of 13 GeV/c and the CERN experiment [5] with that of 19 GeV/c can be available. The invariant mass of $M(K^+\pi^-\pi^-)$ and $M(K^+\pi^-)$ were checked by the BNL and CERN data, respectively. The absolute value of the background around the D^{*-} mass region ($\pm$20 MeV) is reported by the BNL data. In addition, there are the cross section data of the charged track multiplicity [6, 7].

For the simulation of the BNL experiment, the experimental conditions and event se-

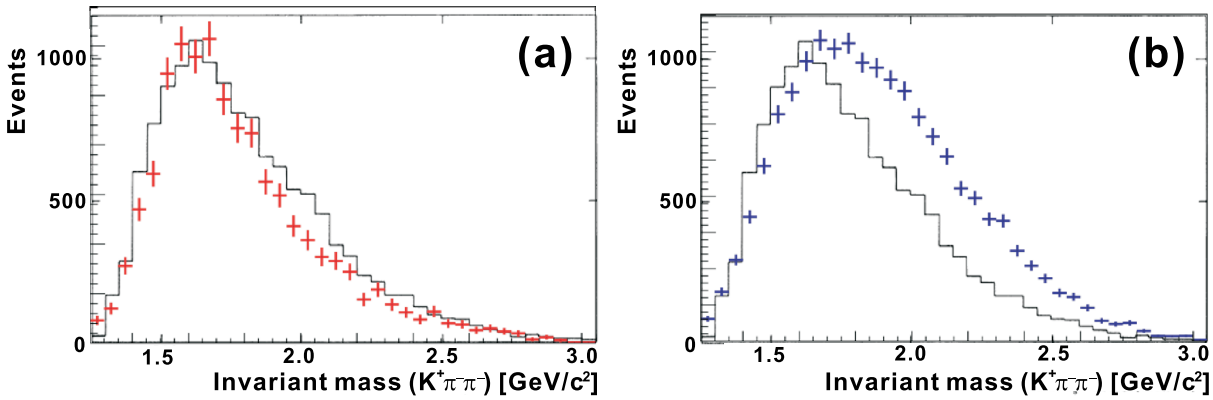

FIG. 1: The simulation results of the invariant mass ($M(K^+\pi^-\pi^-)$) of the BNL data by JAM(a) and PYTHIA(b). The black line shows the experimental background shape. The overlapping red and blue crosses are simulated shapes by JAM and PYTHIA, respectively. The maximum positions are normalized to the data.

lections were taken into account to obtain the invariant mass spectrum. The detail of the simulation conditions are described in Appendix A. Figure 1(a) shows the invariant mass spectrum generated by the simulation, overlapping on the spectrum obtained from the BNL experiment. We found that the experimental data was almost reproduced by the JAM simulation. The same simulation was performed by the PYTHIA code. The result shows the different background shape in Fig. 1(b). The absolute value of the experimental data was reported to be 230±15 counts (stat. error) around the D^{*-} mass region (±20 MeV). From the JAM simulation, the absolute value was estimated to be 240±50 counts (stat.+syst. error). It was found that the JAM code had the small ambiguity of $20-30\%$. On the other hand, the events in the higher mass region by the PYTHIA simulation was larger than that of the data and JAM. The absolute value was estimated to be 1000±110 counts (stat.+syst. error).

Figure 2 shows the simulation results of the CERN experimental data. The background shapes were almost reproduced by both JAM (Fig. 2(a)) and PYTHIA (Fig. 2(b)). The ratio between the background events from the $K^*(890)^0$ production and the high mass tail was almost reproduced. The shape of the experimental data was mainly determined by the production ratio between the $K^*(890)^0$ production and the other K^+ productions. Both JAM and PYTHIA have the similar input parameters to reproduce the production ratio. The absolute value of the experiment was not clear so that the absolute counts around the $\bar{D}^0$ mass was not compared. The detail of the simulation conditions are described in Appendix B.

In addition, the cross section data of the charged track multiplicity were checked in Table.I−III. The cross sections were reproduced with the small difference by both simulations. In detail, the PYTHIA gives the smaller charged track multiplicity from the other

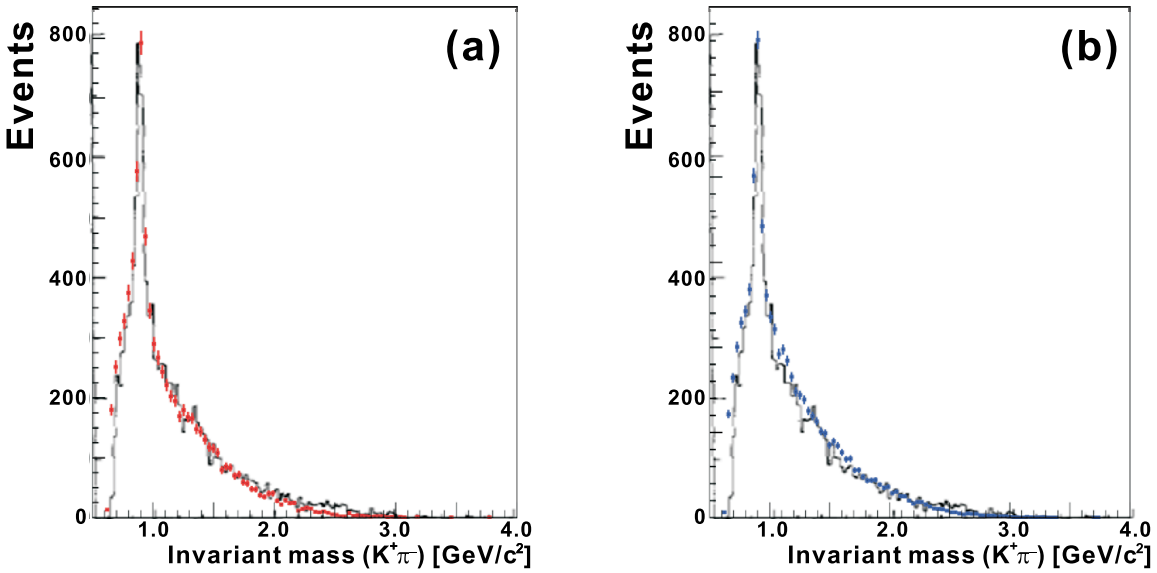

FIG. 2: The simulation results of the invariant mass ($M(K^+\pi^-)$) of the CERN data by JAM(a) and PYTHIA(b). The black line shows the experimental background shape. The overlapping red and blue crosses are simulated shapes by JAM and PYTHIA, respectively. The maximum positions ($K^*(890)$ resonance peak) are normalized to the data.

results. The track multiplicity including neutral tracks by PYTHIA was smaller than that of JAM.

It was found that both simulators have an ambiguity within only a factor from the experimental data. The energy dependence of the cross section in the region of $4 < \sqrt{s} < 10$ GeV has no structure because there are no particular contributions from the resonances to produce the background particles. Therefore, the backgrounds by both simulators were well reproduced with a small ambiguity. The tendency of the PYTHIA simulation was found that the number of events in the high-mass region was larger than than that of data and JAM. This larger contribution in the high-mass region was due to the different parameterizations of the hadronization processes. When the contributions of the non-resonant processes are

TABLE I: The experimental cross section of the charged track multiplicity of the $\pi^- p \to X$ reaction from data and the JAM and PYTHIA simulation.

Number of tracks	2T [mb]	4T [mb]	6T [mb]	8T [mb]	10T [mb]	Total [mb]
Data	9.8	9.0	4.9	1.4	0.2	25.2
JAM	8.0	8.8	6.2	1.4	0.1	24.5
PYTHIA	8.8	9.7	5.2	0.8	0.1	24.6

TABLE II: The experimental cross section of the charged track multiplicity of the $\pi^- p \to \Lambda X$ reaction from data and the JAM and PYTHIA simulation.

Number of tracks	2T [μb]	4T [μb]	6T [μb]	8T [μb]	10T [μb]	Total [μb]
Data	466	480	200	26.6	1.80	1174
JAM	363	482	155	9.00	0.02	1009
PYTHIA	509	549	127	5.84	0.05	1191

TABLE III: The experimental cross section of the charged track multiplicity of the $\pi^- p \to K^0 X$ reaction from data and the JAM and PYTHIA simulation.

Number of tracks	2T [μb]	4T [μb]	6T [μb]	8T [μb]	10T [μb]	Total [μb]
Data	714	787	266	45.2	2.4	1815
JAM	810	1069	345	23.8	0.2	2248
PYTHIA	960	1203	302	13.1	0.1	2478

larger, the invariant mass is shifted to be higher mass region due to the higher probability to generate the combinations of more energetic particles. In addition, by selecting the soft π^- for the D^* tagging method, the probability to generate the combinations of energetic particles becomes higher. The smaller number of the track multiplicity of PYTHIA than that of JAM gives the same tendency from the PYTHIA simulation. In the case of the JAM code, the parametrization of the hadronization process in this energy region was tuned by using the BNL heavy iron collision data whose energy was 14 GeV/A. The similar tuning condition gives the better reproducibility of JAM than that of PYTHIA. On the other hand, the contribution of the hard scattering process were negligible. When the switches of the hard processes were turned off to both JAM and PYTHIA, the results had no difference. The main contributions are the soft processes.

Background reduction

The reduction of those three kind of the background processes were studied by the simulation.

- Strangeness production backgrounds which include the final state particles of the (K^+, π^-, π^-) mode
- Wrong particle identification to the final state particles such as the (π^+, π^-, π^-) and (p, π^-, π^-) modes

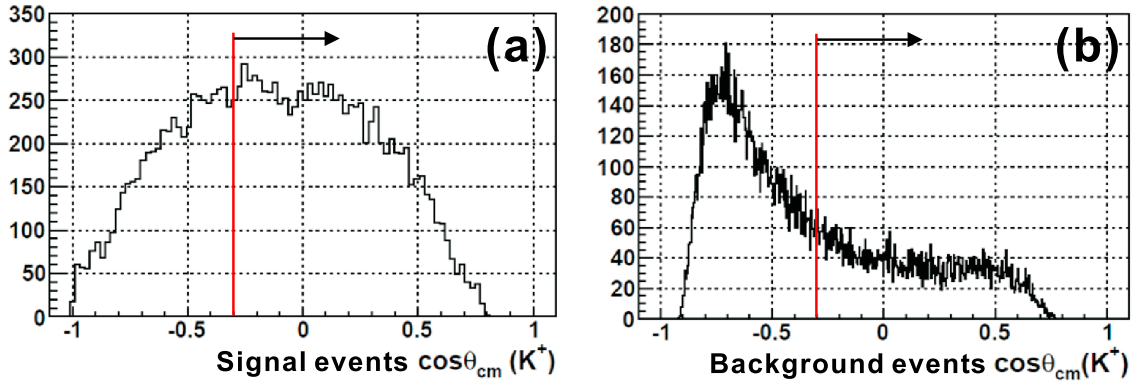

FIG. 3: The angular distribution of K^+ in the center-of-mass system. Figure.(a) and Figure.(b) show the distribution of the signal and background events including the spectrometer acceptance, respectively. The selected regions are indicated by the arrow.

- Associated charm productions which produce the D^{*-} meson

The main method of the background reduction is the D^* tagging. Both the mass region of the $\bar{D}^0$ mass and the Q-value ($Q = M(K^+\pi^-\pi^-) - M(K^+\pi^-) - M_{\pi^-}$) corresponded to the D^{*-} decay are selected. By using the D^* tagging, the background reduction of 2×10^6 can be achieved by the JAM simulation. Although the background level is still high by only using the D^* tagging, the other background reduction methods are applied for the farther background reduction.

One method is the angular selection of the K^+ and π^- in the center-of-mass system. The invariant mass of $\bar{D}^0$ is reconstructed by the detected K^+ and π^-. When we go back to the center of mass system of K^+ and π^-, the angular distributions in the CM system are different between the $\bar{D}^0$ decay particle events and the background ones. The K^+ and π^- from the $\bar{D}^0$ decay are commonly boosted to the momentum direction of $\bar{D}^0$ and both of them are energetic. Thus, the angular distributions in the center-of-mass system turn to be symmetric because of the balance of the K^+ and π^- energy. On the other hand, the angular distributions of the K^+ and π^- from the background turn to be asymmetric because the events which have the unbalance K^+ and π^- energy can make the invariant mass of $\bar{D}^0$. Therefore, the angular distributions of K^+ and π^- should be localized around $\cos\theta_{CM} = \pm 1$ in the center of the mass system as shown in Fig 3(b). Although the true signal events are decreased to be 0.58 by using the scattering angle selection in the center-of-mass system, the background reduction of 3.8 can be achieved. The S/N ratio improved to be 2.2. The angular distribution of the background K^+ in the center-of-mass system is localized to $\cos\theta_{CM} = -1$. It means that the combinations between the higher momentum π^- and the low momentum K^+ reconstruct the $\bar{D}^0$ mass, because the production rate of π^-

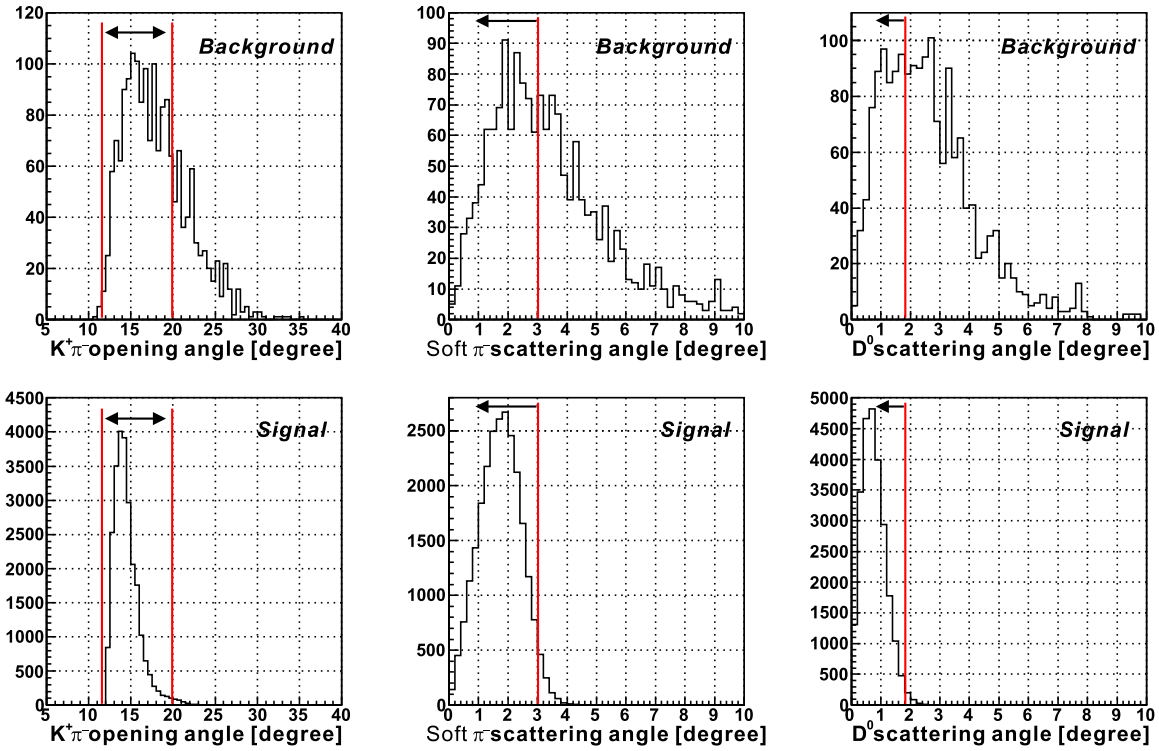

FIG. 4: The examples of the event selections, the opening angle of K^+ and π^- and the scattered angle of $\bar{D}^0$ and π^- from the D^{*-} decay. The selected regions are indicated by the arrow.

is 10 times larger than that of K^+.

For reducing more background, the event selections by using the kinematical conditions of the $\pi^- + p \to Y_c^{*+} + D^{*-}$ reaction were used. From the study of the production cross section, the t-channel process is found to be dominant so that the scattered particles from the D^{*-} decay have very forward angular distributions. Figure 4 shows the examples of the event selections. By selecting the forward direction of the scattered angle of $\bar{D}^0$ and π^- from the D^{*-}decay, the opening angle of K^+ and π^- from the $\bar{D}^0$ and that of $\bar{D}^0$ and π^-, and the possible other event selections, the background reduction of 4.1 can be achieved.

In addition, to identify the strangeness production events such as Λ and K_S^0 by analyzing the different combination of pions which reconstructed the D^{*-} events, the displayed vertex method can be used to reduce the background. The signal events was not rejected by this analysis because the pions from the true D^{*-} events can not reconstruct the mass of Λ and K_S^0. Although this analysis method strongly depends on the production ratio of those special channels, by requiring the vertex point of the D^{*-} production, 20−30% of the background events can be rejected.

Combining the scattering angle selection of the K^+, π^- in the center-of-mass system and the other possible event selections, the reduction of 15 and the S/N ration of 10 can be

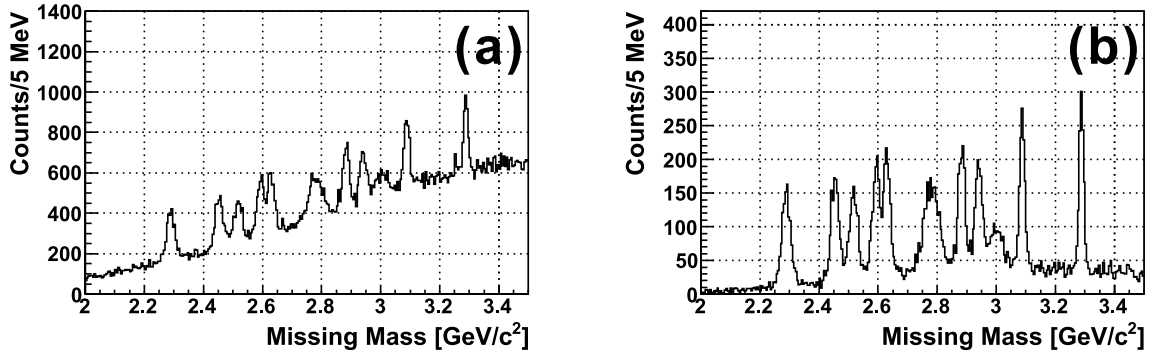

FIG. 5: The missing mass spectra with the background reduced only by the D^* tagging (a) and by the the D^* tagging with the possible event selections (b).

achieved. The main background was reduced to be ∼6000 counts in the missing mass region of $2.2 - 3.4$ GeV/c^2. The average background level reduced to be 5 counts/MeV as shown in Fig. 5.

In the case of the PYTHIA simulation, the total reduction factor was 2.3 times worse. The reduction of the D^* tagging is worse than that of the JAM simulation. The reduction by the event selections were the same as of JAM. Therefore, we found that the ambiguity from the different Monte-Carlo code is a factor of 2.

Background reduction of the wrong particle identification

Due to the performance of the PID counter, it is necessary to study the background contributions of the wrong particle identification (miss-PID) to the final state particles. The main contribution of the miss-PID is the final state of the (π^+, π^-, π^-) and (p, π^-, π^-) modes. Considering the conventional RICH system, the miss-PID rate is estimated to be a few percent level. The result of the background level with the D^* tagging and the event selection shows that the contribution of the (π^+, π^-, π^-) and (p, π^-, π^-) modes are ∼970 and ∼1600 counts per 1% miss-PID, respectively. By assuming 3% of miss-PID, the contribution of the background is ∼7700 counts in the missing mass region of $2.2 - 3.4$ GeV/c^2. The average background level by miss-PID is 6 counts/MeV. The detail of the simulation conditions and the contribution from the other channels are described in Appendix C.

Background reduction of the associated charm production

The background contributions of the associated charm production are studied as following.

- Highly excited D^* production (the D^{**} production)

- Non-resonant $D^{*-} + \pi$ production
- Non-resonant $D\bar{D}$ pair production
- $c\bar{c}$ meson production (M($c\bar{c}$))

By using the D^* tagging method, the reaction channels including D^{*-} only remain in the missing mass spectrum. Although the associated charm production events could not be rejected by only the D^* tagging, a large part of those production were reduced by the event selections due to the different kinematical conditions. The production cross sections of the associated processes were assumed to be 1 nb for each channel. By taking into account the reaction channels, the events with the total cross sections of 9 nb, 4 nb, 4 nb and 12 nb were generated for the D^{**} production, the non-resonant $D^{*-} + \pi$ production, the non-resonant $D\bar{D}$ pair production and the $c\bar{c}$ meson production, respectively. The events which remained in the missing mass spectrum were ∼1900 counts with the continuum spectrum shape. The D^{**} production events mainly contribute to the background.

In the real experiment, the origin from D^{*-} can be checked by analyzing the correlations and kinematical conditions. For the D^{**} production, the production rate of the D^{**} mesons were obtained by reconstructing the mass. The contribution and the background shape can be estimated from the data. For the other backgrounds, by changing of the momentum and the scattering angle of D^{*-} from the associated events, the positions and the background shape in the missing mass spectrum were also changed. Those possible peaking background sources can be identified The contribution by the associated charm production was found to be minor.

The detail of the simulation conditions and the checked channels are described in Appendix D.

Sensitivity

Figure 6 shows the missing mass spectrum with the simulated backgrounds. From the background level with the strangeness background, the wrong particle identification and the associated charm production, the sensitivity of the charmed baryon production was estimated. The 3σ sensitivity for the Λ_c^+ production with the mass resolution of 16 MeV(rms) was estimated to be 0.05 nb for the 2.5σ peak region. For the higher excited region more than 2.8 GeV/c^2, by assuming the Breit Wigner peak shape with the 95% region, the 3σ sensitivity of $\sigma_{tot.}$ =0.12−0.16 nb and ∼0.25 nb can be achieved for Y_c^* with $\Gamma = 10-30$ MeV and $\Gamma \sim 100$ MeV, respectively. The sensitivity was obtained from the square root of counts in the 95% region of the Breit Wigner peak compared with the event counts of the charmed baryons. Since those cross section values are only considered with the statistical errors of the background spectrum, by taking into account the ambiguity of the JAM and PYTHIA codes, the sensitivity becomes 1.5 time worse. Figure **??** shows the missing mass spectrum

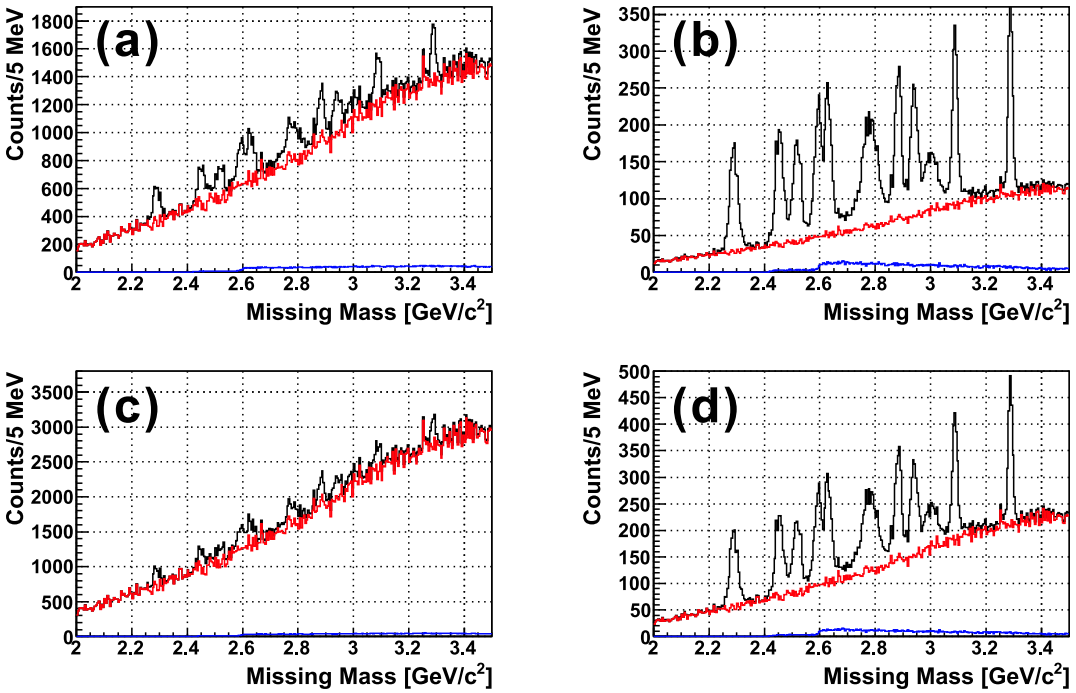

FIG. 6: The missing mass spectra with the background reduced only by the D^* tagging (a,c) and by the the D^* tagging with the possible event selections (b,d). (a,b) shows the simulation results by the JAM code and (c,d) shows that of the PYTHIA code. The black line shows the sum spectrum with the Y_c^* signal of 1 nb case for each peak. The red and blue lines show the background spectra from the strangeness production combined with the wrong particle identification and the associated charm productions, respectively.

by taking into account the ratio of the cross section of Y_c^{*+}. The Λ_c excitation states can be clearly observed, while the Σ_c states have the low sensitivity. However, the production ratio between Λ_c and Σ_c states can be compared from the missing mass spectrum.

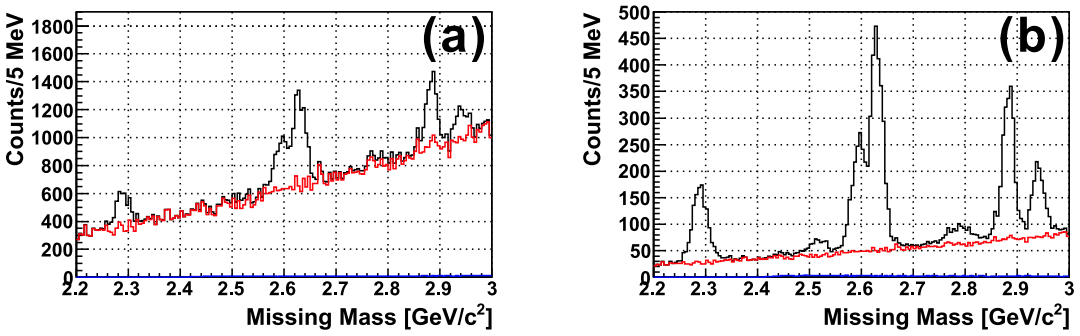

FIG. 7: The missing mass spectra with the background reduced only by the D^* tagging (a) and by the the D^* tagging with the possible event selections (b). The cross section ratio of Y_c^{*+} was taken into account in the spectrum. The red and blue lines show the background spectra from the strangeness production combined with the wrong particle identification and the associated charm productions, respectively.

2. Decay measurement

Spectrometer setup modification

The magnetic spectrometer system was modified for both the missing mass and the decay measurement. In the case of the fixed target experiment with the higher momentum beam, all the generated particles, not only the scattered high-momentum particles from the D^{*-} decay but also the decay products from the produced Y_c^{*+}, are scattered to the forward direction. Therefore, the dipole magnet system which commonly measures both the particles from the D^{*-} decay for the missing mass method and the decay products from the produced Y_c^{*+} for the decay measurement was designed. The modified points of the spectrometer setup are following.

- The target position was moved to as close to the magnet as possible by keeping the invariant mass resolution ($M(K^+\pi^-)$).
- The larger size of the internal tracking detectors were installed.
- The surrounding detectors were installed around the magnet pole peace for horizontally measuring the decay π^- from D^{*-} and the decay products from Y_c^{*+}.
- The pole pad-type detector were installed on the face of the magnet pole for vertically measuring the decay products from Y_c^{*+}.

Figure 8 shows the modified spectrometer system. The performances of the spectrometer was also changed by the modification. The detail of the performances are described in Appendix E.

For the decay measurement with the wider angular coverage, it is necessary to detect the decay products at just the downstream of the target position. The tracking detectors which have the larger angular acceptance were installed at the downstream of the target. The horizontal direction can be covered by using the detectors installed around the magnet pole. The coverage for the polar angle is $\cos\theta_{CM} > -0.9$ for the $\Lambda_c(2940)^+ \to \Sigma_c(2455)^{++,0} + \pi^{-,+}$ decay angle in the center-of-mass frame. However, by only covering the horizontal direction, the sensitivity of the measurement for the azimuthal angle is lost. For covering the vertical direction, the detector which has at least the function to measure the timing information has to be installed on the magnet pole face. By using the pole pad-type detector, the vertical direction can be covered ($\cos\theta_{CM} > -0.5$). As shown in Fig. 9, both the polar and azimuthal angle are completely covered more than $\cos\theta_{CM} = -0.5$ for the $\Lambda_c(2940)^+ \to \Sigma_c(2455)^{++,0} + \pi^{-,+}$ decay mode.

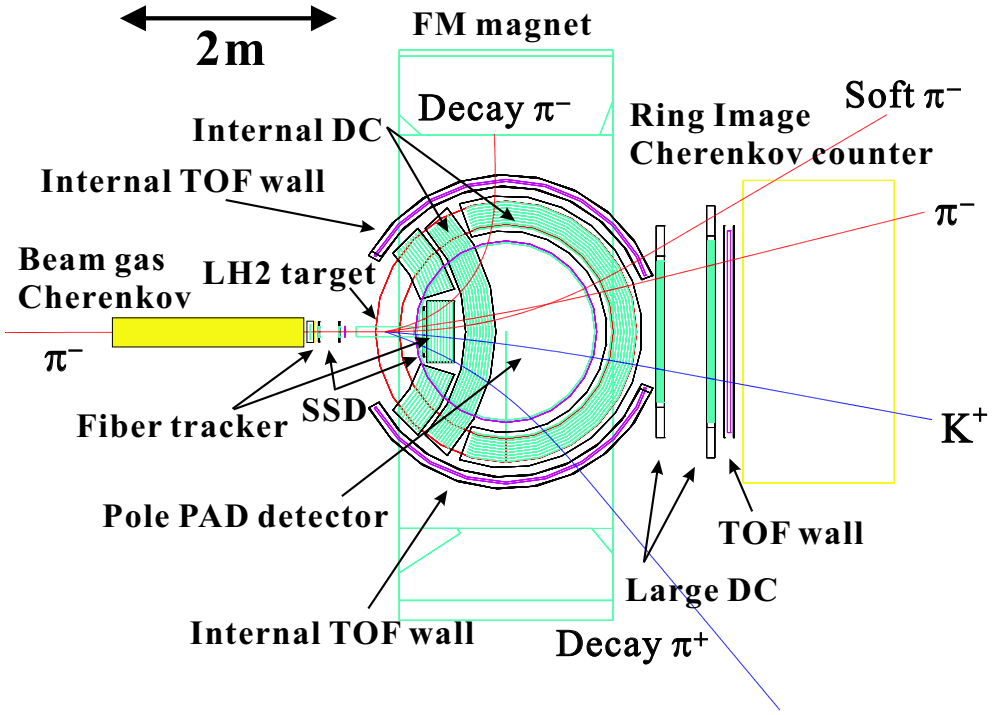

FIG. 8: The schematic view of the modified spectrometer system.

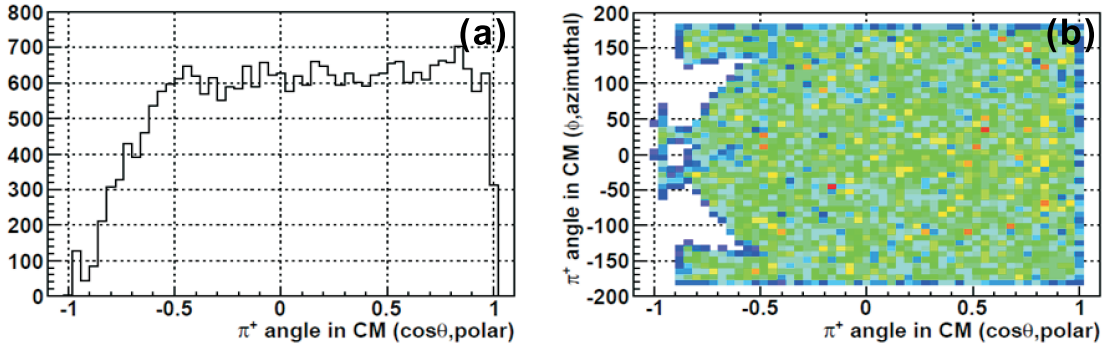

FIG. 9: The detected decay angular distribution of the $\Lambda_c(2940)^+ \to \Sigma_c(2455)^{++,0} + \pi^{-,+}$ mode in the center-of-mass frame. (a) and (b) show the polar angle distribution and the correlation between polar and azimuthal angle, respectively.

Missing mass spectra from charmed baryon decay

The decay measurement is necessary to study the structure of the charmed baryon. The branching ratio between $\Sigma_c + \pi$ and $N + D$ is important to study the di-quark nature of the charmed baryon. The measurements of the decay angular distribution of the decay particles

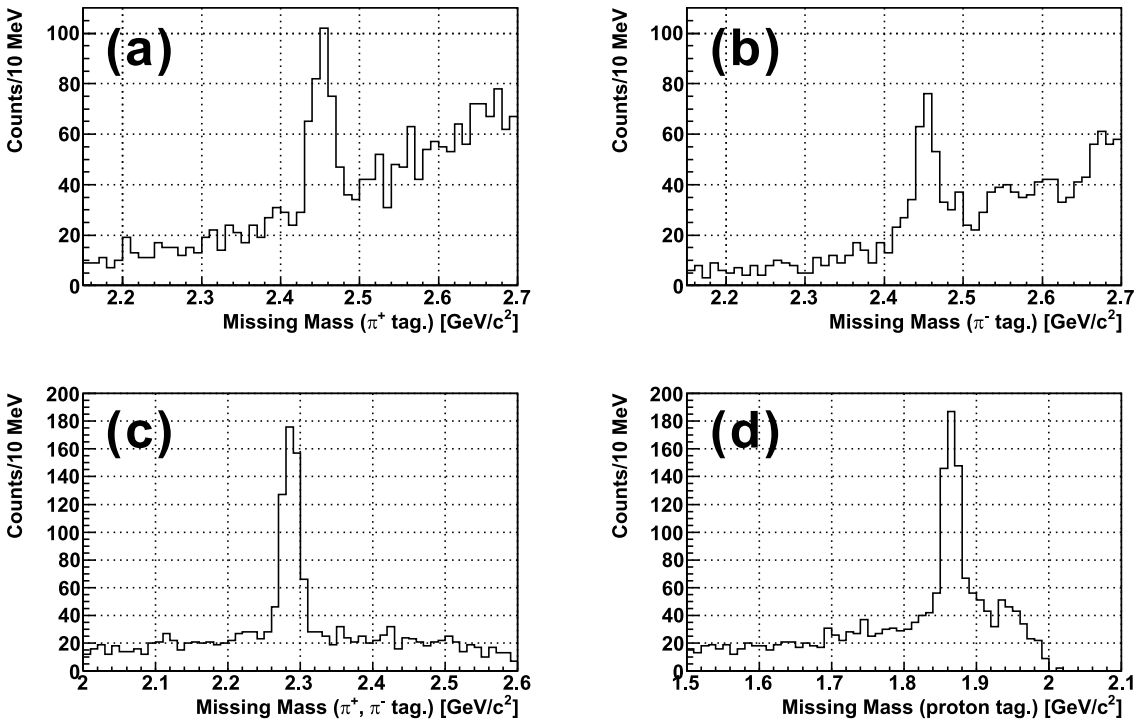

FIG. 10: The missing mass spectra by tagging the decay products from $\Lambda_c(2940)^+$. (a), (b), (c) and (d) show the decay mode of $\Sigma_c(2445)^0 + \pi^+$, $\Sigma_c(2445)^{++} + \pi^-$, $\Lambda_c^+ + \pi^+ + \pi^-$ and $p + D^0$, respectively.

and branching ratio between $\Sigma_c(2455)+\pi$ and $\Sigma_c(2520)+\pi$ are also inseparable to determine the spin-parity of the produced state.

For those studies, the performance of the decay measurement was checked by using the EvtGen code [8]. The decay mode of $\Lambda_c(2940)^+$ are artificially input in the simulation code as following.

- Γ_{N+D} =0.40: $\Gamma_{pD^0} = 0.20$ and $\Gamma_{nD^+} = 0.20$
- $\Gamma_{\Sigma_c+\pi}$ =0.40: $\Gamma_{\Sigma_c(2445)^{++}\pi^-} = 0.13$, $\Gamma_{\Sigma_c(2445)^+\pi^0} = 0.13$ and $\Gamma_{\Sigma_c(2445)^0\pi^+} = 0.13$
- $\Gamma_{\Lambda_c+\pi+\pi}$ =0.20: $\Gamma_{\Lambda_c^+\pi^+\pi^-} = 0.10$ and $\Gamma_{\Lambda_c^+\pi^0\pi^0} = 0.10$

The recoil momentum of Y_c^{*+} is measured by the missing mass method so that the mass of the decay products ($\Sigma_c(2455)^{++,0}$ and D^0) can be obtained by only detecting the emitted pions and protons. The mass of the decay daughter can be measured for those a few body decay modes, $\Sigma_c(2445)^0+\pi^+$, $\Sigma_c(2445)^{++}+\pi^-$, $\Lambda_c^+ + \pi^+ + \pi^-$ and $p+D^0$. The missing mass spectra by tagging the decay products have clear peak as shown in Fig. 10. The missing mass region of $\pm$30 MeV around the $\Lambda_c(2940)^+$ mass was selected.

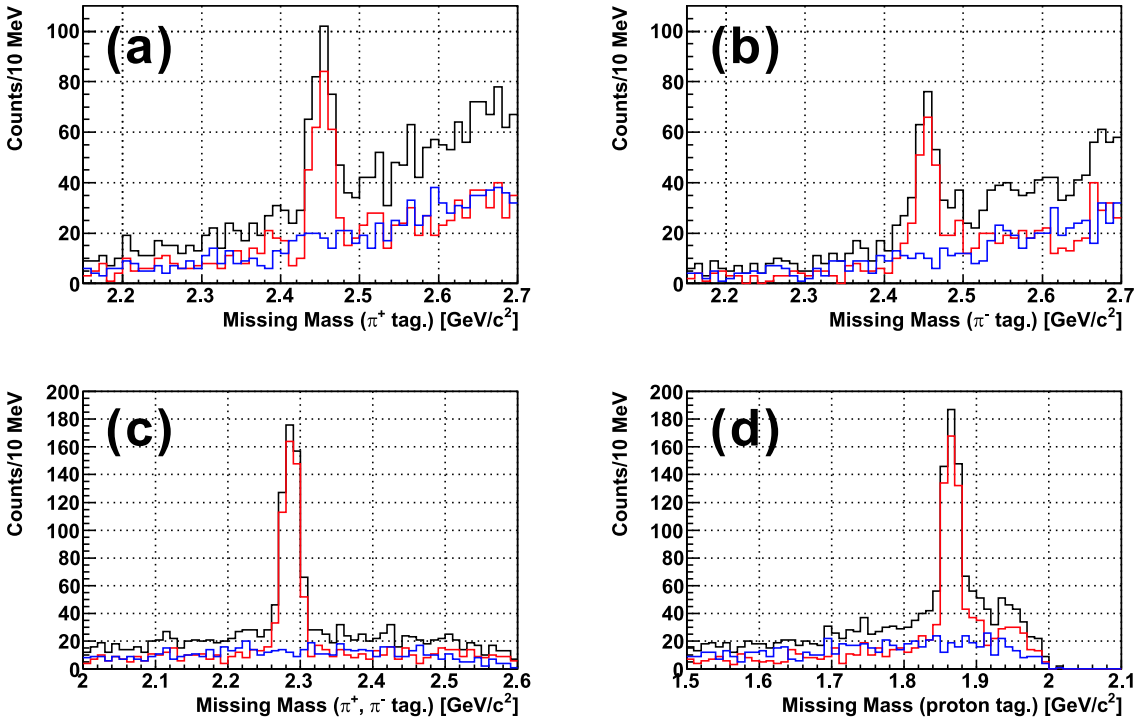

FIG. 11: The missing mass spectra by tagging the decay products from $\Lambda_c(2940)^+$ including the strangeness production background. (a), (b), (c) and (d) show the decay mode of $\Sigma_c(2445)^0 + \pi^+$, $\Sigma_c(2445)^{++} + \pi^-$, $\Lambda_c^+ + \pi^+ + \pi^-$ and $p + D^0$, respectively. The black, red, blue lines are the sum spectra, the charmed baryon decay events and the strangeness production background, respectively.

Figure 11 shows the contribution from each background sources. The background sources were the decay products of the charmed hadrons such as Λ_c^+ and $D^{+,0}$ and the strangeness production and the wrong particle identification. The contributions of event from the strangeness production and the wrong particle identification were the same that from the charmed baryon decays. The detail of the background events from the decay products of the charmed hadrons are described in Appendix F.

By gating the Λ_c^+ mass region in the $\pi^\pm$ tagging events, those background can drastically be decreased as shown in Fig. 12. By this selection, the loss of the charmed baryon decay is only $\sim$10%. The decay chain analysis can be performed with the low background level.

To increase the number of decay events, the 4-body mode ($\bar{D}^0 \to K^+ + \pi^- + \pi^+ + \pi^-$) was analyzed. By including the event from the 4-body decay mode, the amount of events can be increased to be 3 times due to the larger branching ratio. The detail of simulation are described in Appendix F 1.

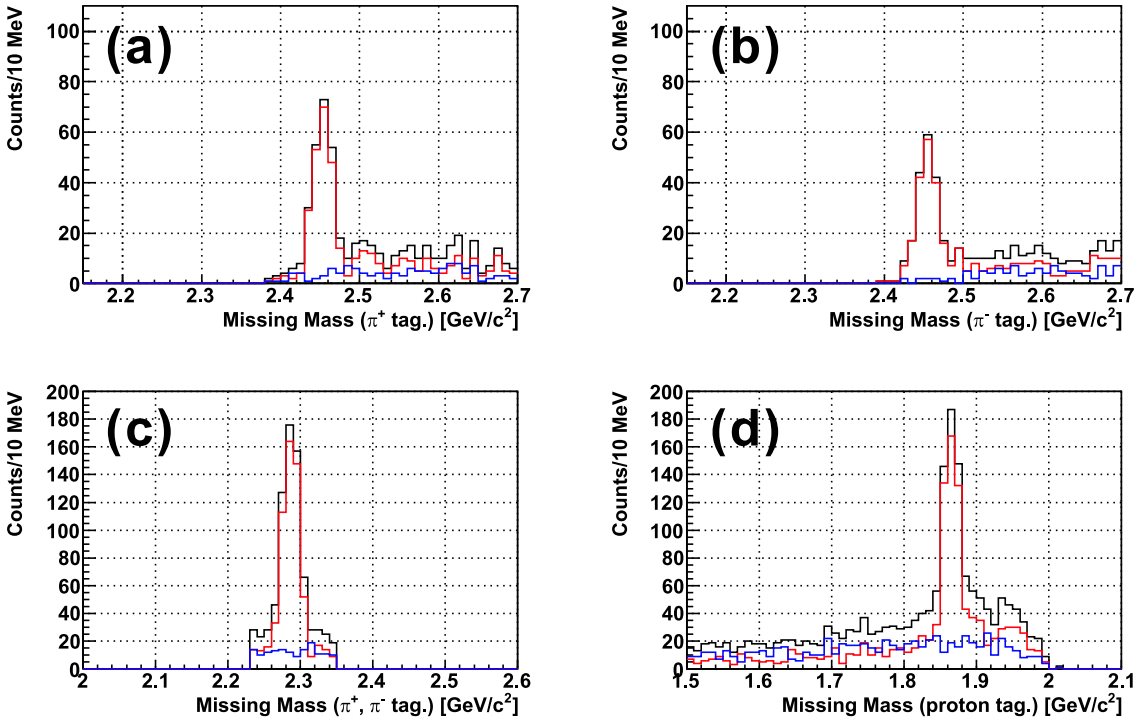

FIG. 12: The missing mass spectra by tagging the decay products from $\Lambda_c(2940)^+$ including the strangeness production background and by gating the Λ_c^+ mass region in the $\pi^\pm$ tagging events. (a), (b), (c) and (d) show the decay mode of $\Sigma_c(2445)^0 + \pi^+$, $\Sigma_c(2445)^{++} + \pi^-$, $\Lambda_c^+ + \pi^+ + \pi^-$ and $p + D^0$, respectively. The black, red, blue lines are the sum spectra, the charmed baryon decay events and the strangeness production background, respectively.

Number of events which can be used for the decay measurement

The number of events of the $\Sigma_c^{++,0}\pi^{-,+}$ and $p + D^0$ channels combined with both 2-body and 4-body mode are ∼550 and ∼870 counts, respectively. The branching ration can be determined by the statistical error of less than 5% with the assuming branching ratio in the case of 1 nb production cross section. The sensitivities of the decay measurement for the $\Sigma_c + \pi$ and $p + D^0$ modes were estimated to be $\Gamma_{\Sigma_c\pi}$ =0.03 and Γ_{pD^0} =0.05, respectively. The angular distribution can be also measured by using those number of events.

For detecting the other channel such as π^0 emitting mode, the calorimeter arrays have to be installed to the spectrometer. The array could be installed around target region, the downstream of the RICH detector and the behind of the internal TOF wall. The coverage of the polar angle was $\cos\theta_{CM} > -0.9$ for the $\Lambda_c(2940)^+ \to \Sigma_c(2455)^0 + \pi^0$ decay angle in the center-of-mass frame. Since the decay γ rays from π^0 which hit to the magnet pole face cannot be detected, there are acceptance loss for the azimuthal angle.

Appendix A: Simulation conditions of the BNL experiment

In the BNL experiment, those experimental conditions were considered to obtained the invariant mass.

- Momentum selection determined by the acceptance, the trigger and the PID counters: $p_K = 2.0 - 8.0$ GeV/c, $p_\pi > 2.0$ GeV/c, $p_{soft\ pi^-} = 0.5 - 1.0$ GeV/c and $p_K + p_\pi > 6.0$ GeV/c
- Q-value selection: $3.2 < Q < 8.2$ MeV, $Q = M(K^+\pi^-\pi^-) - M(K^+\pi^-) - M_{\pi^-}$
- Detector acceptance conditions: Opening angle between K^+ and π^-, horizontal scattering angle (dx/dz) of K^+ and π^-

In the experiment, the high-intensity beam was used and the detectors in which areas the beam passed through were inactive to measure the scattered particles in Fig. 13. Thus, the acceptance hole of the inactive areas has to be considered for the estimation. From the geometrical size, the range of the opening angle between K^+ and π^- was $15° - 18°$ and that of the horizontal scattering angle (dx/dz) of K^+ and π^- was $0.13 - 0.16$. The event selection by the acceptance hole is the most important condition to reproduce the background shape. Since the effects of the acceptance hole was not completely clear by the rack of the information of the geometry, the ranges of the event selection were regraded as systematic errors. Figure 14 and Fig. 15 show the invariant mass shape by changing the event selection conditions. For reproducing the background shape, the opening angle between K^+ and π^- of 17° and the horizontal scattering angle (dx/dz) for K^+ and π^- of 0.15 were selected.

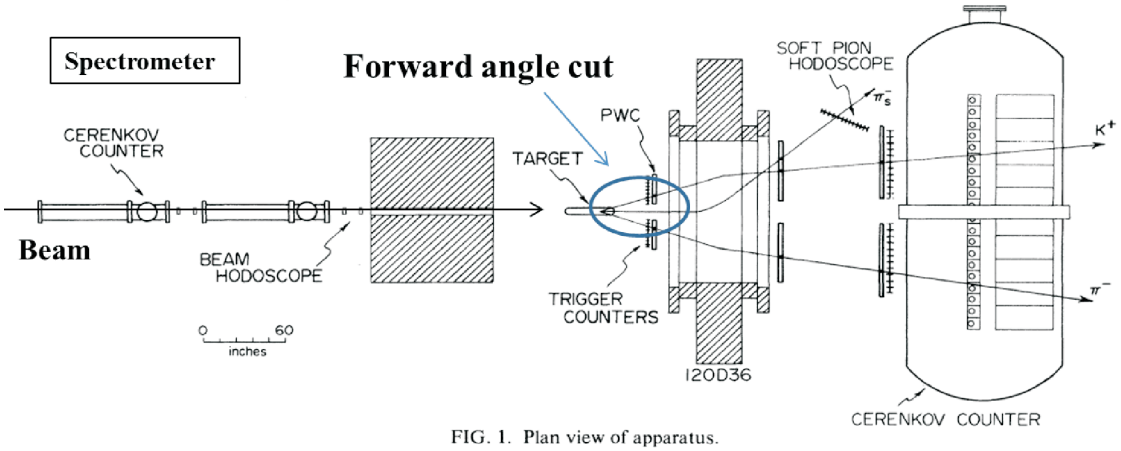

FIG. 1. Plan view of apparatus.

FIG. 13: The setup of the BNL spectrometer system. In the simulation, the acceptance hole was mainly considered to reproduce the background shape.

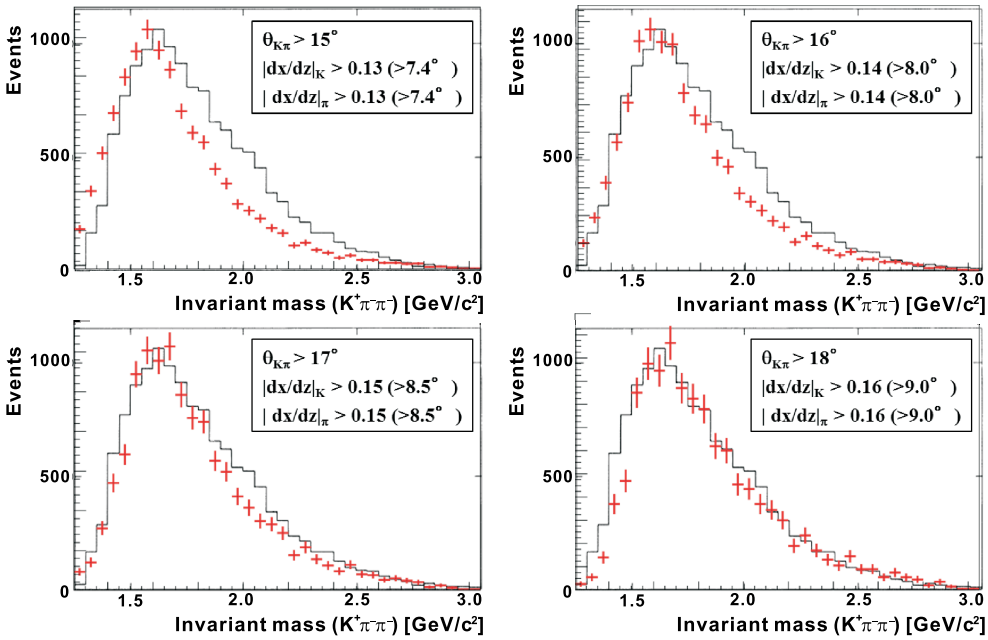

FIG. 14: The background shapes produced by the JAM code by changing the forward scattering angle region. The black line and red crosses show the experimental data and the JAM simulation background, respectively.

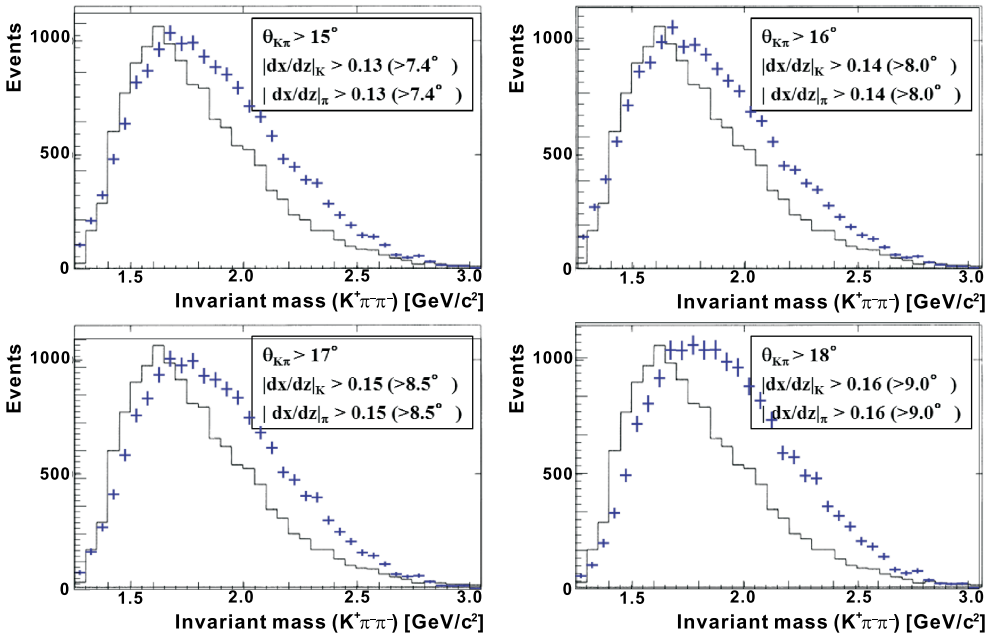

FIG. 15: The background shapes produced by the PYTHIA code by changing the forward scattering angle region. The black line and blue crosses show the experimental data and the PYTHIA simulation background, respectively.

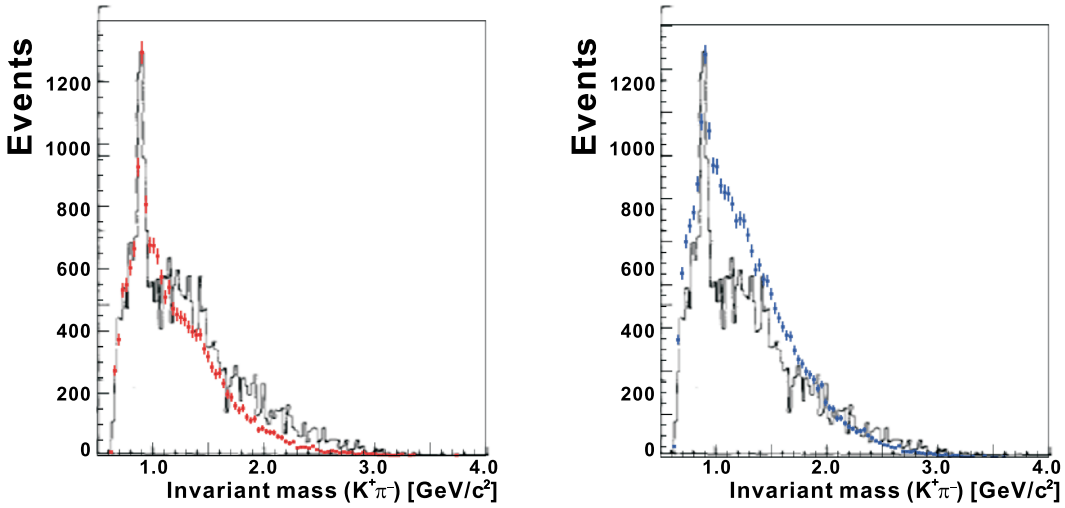

FIG. 16: The simulation results of the invariant mass ($M(K^-\pi^+)$) of the CERN data by JAM and PYTHIA. The black line shows the experimental background shape. The overlapping red and blue crosses are simulated shape by JAM and PYTHIA, respectively. The maximum positions ($K^*(890)$ resonance peak) are normalized to the data.

Appendix B: Simulation conditions of the CERN experiment

In the CERN experiment, those experimental conditions were considered to obtained the invariant mass.

- K^- trigger condition: K^- momentum selection of $3-10$ GeV/c by the PID counter and $p_T > 0.5$ GeV/c by the analysis
- K^+ trigger condition: K^+ momentum selection of $3-10$ GeV/c by the PID counter
- To analyze 6-particle event ($\pi^- p \to \Lambda_c^+ D^-$, $\Lambda_c^+ \to pK^-\pi^+$ and $D^- \to K^+\pi^-\pi^-$): $n_{K^+} = 1$, $n_{K^-} = 1$, $n_{\pi^+} = 1$, $n_{pi^-} = 2$ and $n_p = 1$

Both the invariant mass of $M(K^+\pi^-)$ and $M(K^-\pi^+)$ were checked. The invariant mass of $M(K^+\pi^-)$ was shown in Fig 2. The invariant mass of $M(K^-\pi^+)$ was shown in Fig 16 and Fig 17. The JAM code almost reproduced the background shape. On the other hand, In the case of the PYTHIA code, the ratio between the $\bar{K}^*$ production and the other K^- events was different from the experimental data. By changing the normalized position from the peak position to the tail region, the higher-mass tail can be reproduced by PYTHIA.

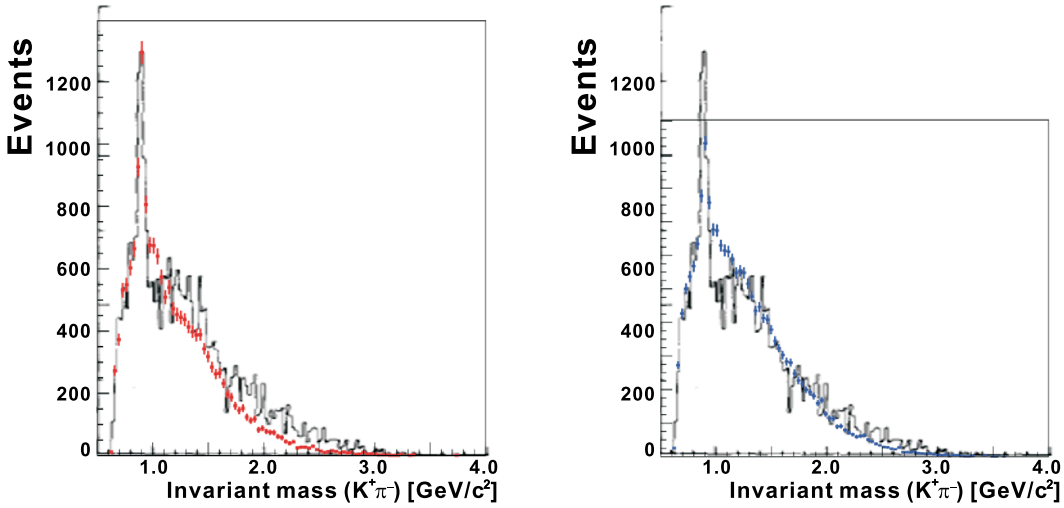

FIG. 17: The simulation results of the invariant mass ($M(K^-\pi^+)$) of the CERN data by JAM and PYTHIA. The black line shows the experimental background shape. The overlapping red and blue crosses are simulated shape by JAM and PYTHIA, respectively. The low-mass tail regions are normalized to the data.

Appendix C: Background reduction for the wrong particle identification

The main contribution of the miss-PID is the final state of the (π^+, π^-, π^-) and (p, π^-, π^-) modes. The production cross sections of the (π^+, π^-, π^-) and (p, π^-, π^-) modes by JAM are 17.4 mb and 10.7 m, respectively, while that of the (K^+, π^-, π^-) is 2.43 mb.

The contribution from the other channels such as (K^+, K^-, π^-), (K^+, π^-, K^-) and (π^+, K^-, π^-) are small due to the small production rate compared with π^-. The contribution of the miss-PID from the higher momentum π^- detected by the RICH counter is small because the production rate of the K^- (5.8%) and $\bar{p}$ (1.9%) is much smaller than that of π^-. The contribution of the miss-PID from the soft π^- by the internal detectors also is small due to the small production rate of the K^- (4.0%) and $\bar{p}$ (0.3%). The contributions of those π^- miss-PID are negligible.

The spectrometer system cannot distinguish positrons/electrons and muons from pions. The semi-leptonic decay channel such as (K^+, μ^-, π^-) and (K^+, e^-, π^-) include the possible background events. Those channels cannot contribute to the background because those events cannot reconstruct the $\bar{D}^0$ mass.

The possible background events including electron are generated by the γ conversion from the π^0 decay. The conversion rate by the target material is $\sim$1% so that the contribution of the π^0 events is negligible.

Appendix D: Background reduction for the associated charm production

Figure 18 shows the invariant mass spectra of $M(K^+\pi^-)$ and the Q-value ($Q = M(K^+\pi^-\pi^-) - M(K^+\pi^-) - M_{\pi^-}$) including the associated charm production channels, such as the D^{**} production, the non-resonant $D^{*-} + \pi$ production, the non-resonant $D\bar{D}$ pair production and the $c\bar{c}$ meson production. By gating the $\bar{D}^0$ mass region and Q-value corresponded to the D^{*-} decay, only the events including the D^{*-} production remain in the missing mass.

For the D^{**} production, those 9 channels are considered, $\Lambda_c^+ + D^{**-}$, $\Sigma_c^+ + D^{**-}$ and $\Sigma_c^0 + \bar{D}^{**0}$ (D^{**}=$\bar{D}_0^*(2400)$, $\bar{D}_1(2420)$ and $\bar{D}_2^*(2460)$ [9]). The cross sections of each reaction channel are assumed to be 1 nb, $\sigma_{tot.} = 9$ nb. The production angle of the $\pi^- + p \to Y_c + \bar{D}^{**}$ reaction is assumed to be the $exp(bt)$ distribution in the center-of-mass system. Figure 19 show the missing mass spectrum of the D^{**} production events. In the figure, 10 times larger number of events (corresponded to 10 nb/ch case) were generated. The events in the background spectrum is $\sim$1800 counts. This reaction is the largest contribution of the background spectrum. The production rate of the D^{**} mesons can be obtained by reconstructing its mass. The contribution of events and the background shape can be estimated from the data.

For the non-resonant $D^{*-} + \pi$ production, those 4 channels are considered, $\Lambda_c^+ + D^{*-} + \pi^0$,

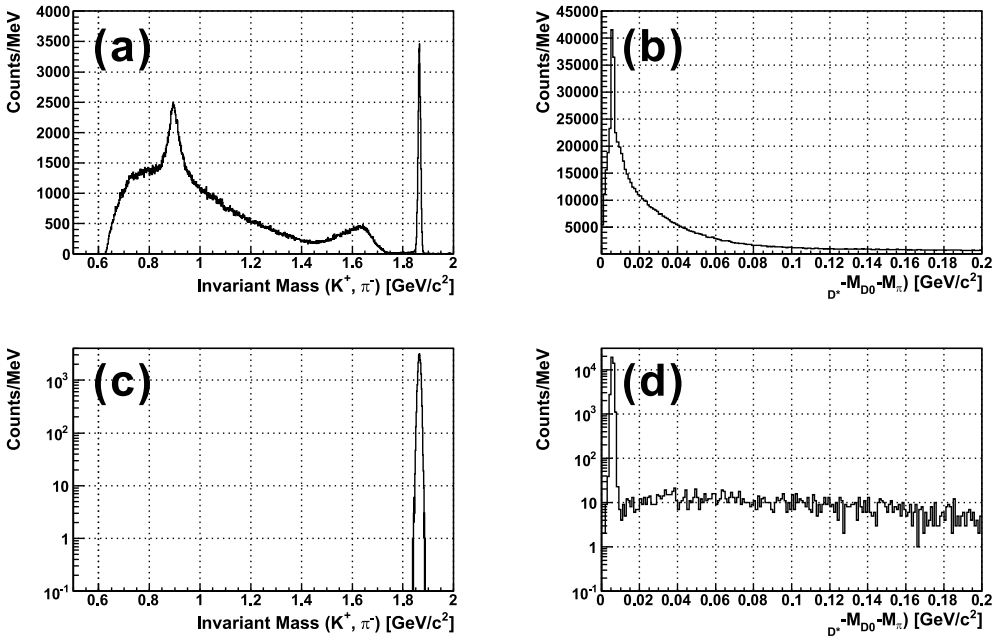

FIG. 18: The invariant mass, $M(K^-\pi^+)$ and the Q-value, $Q = M(K^+\pi^-\pi^-) - M(K^+\pi^-) - M_{\pi^-}$ spectra including the associated charm production channels. (a) and (b) show the inclusive spectra. (c) and (d) show the spectra by gating the $\bar{D}^0$ mass region.

$\Sigma_c^{++}+D^{*-}+\pi^-$, $\Sigma_c^{+}+D^{*-}+\pi^0$ and $\Sigma_c^{0}+D^{*-}+\pi^+$. The cross sections of each reaction channel are assumed to be 1 nb, $\sigma_{tot.} = 4$ nb. The production angle of the $\pi^- + p \to Y_c + D^{*-} + \pi$ reaction is assumed to be isotropic distribution in the center-of-mass system. Figure 20 show the missing mass spectrum of the non-resonant $D^{*-} + \pi$ production events. In the figure, 10 times larger number of events (corresponded to 10 nb/ch case) were generated. The events in the background spectrum is ∼30 counts. The amount events were found to be small so that the events from the non-resonant $D^{*-} + \pi$ production cannot make the structure in the missing mass spectrum. If the cross section was ∼50 times larger case, The events from the non-resonant $D^{*-} + \pi$ production make a structure in the missing mass spectrum. In this case, the production rate of the non-resonant $D^{*-} + \pi$ production can be obtained by detecting pions. The contribution of events and the background shape can be estimated from the data.

For the non-resonant $D\bar{D}$ pair production, those 4 channels are considered, $D^{*+}+D^{*-}+n$, $D^{*0}+D^{*-}+p$, $D^{+}+D^{*-}+n$ and $D^{0}+D^{*-}+p$. The cross sections of each reaction channel are assumed to be 1 nb, $\sigma_{tot.} = 4$ nb. The production angle of the $\pi^- + p \to D + \bar{D} + N$ reaction is assumed to be isotropic distribution in the center-of-mass system. Figure 21 show the missing mass spectrum of the non-resonant $D\bar{D}$ pair production events. In the figure, 10 times larger number of events (corresponded to 10 nb/ch case) were generated. The events

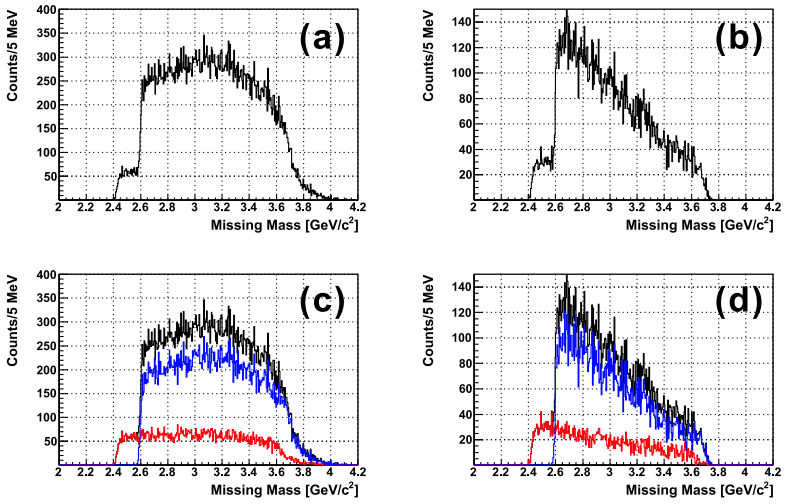

FIG. 19: The missing mass spectra of the D^{**} production events. (a,c) and (b,d) show the spectrum with only the D^* tagging and both the D^* tagging and the event selections by using the kinematical conditions, respectively. The black liens show the sum spectra. The red and blue line show the missing mass spectra from $\Lambda_c^+ + D^{**-}$ and $\Sigma_c^{+,0} + \bar{D}^{**-,0}$, respectively. In the simulation, 10 times larger number of events (corresponded to 10 nb/ch case) were generated.

in the background spectrum is ∼30 counts. The amount events were found to be small so that the events from the non-resonant $D\bar{D}$ pair production cannot make the structure in the missing mass spectrum. If the cross section was ∼20 times larger case, The events from the non-resonant $D\bar{D}$ pair production make a structure in the missing mass spectrum. In this case, by changing the momentum and the scattering angle of D^{*-} from the associated events, the positions and the background shape in the missing mass spectrum were also changed. Those possible peaking background sources can be identified.

For the $c\bar{c}$ meson production, those 12 channels are considered, $\eta_c(1S)$, $\eta_c(2S)$, J/ψ, $\psi(2S)$, $\psi(3770)$, $\psi(4040)$, $\psi(4160)$, $\psi(4415)$, χ_{c0}, χ_{c1}, χ_{c2} and h_c [9]. The cross sections of each reaction channel are assumed to be 1 nb, $\sigma_{tot.} = 12$ nb. The production angle of the $\pi^- + p \to M(c\bar{c}) + n$ reaction is assumed to be the $exp(bt)$ distribution in the center-of-mass system. Figure 22 show the missing mass spectrum of the $c\bar{c}$ meson production events. In the figure, 10 times larger number of events (corresponded to 10 nb/ch case) were generated. The events in the background spectrum is ∼40 counts. Only the $c\bar{c}$ mesons which can decay to $D\bar{D}$ pair ($\psi(4040)$, $\psi(4160)$ and $\psi(4415)$) remain in the background. The amount events were found to be small so that the events from the non-resonant $D\bar{D}$ pair production cannot make the structure in the missing mass spectrum. If the cross section was ∼30 times larger case, The events from the non-resonant $D\bar{D}$ pair production make a structure in the missing mass spectrum. In this case, by changing the momentum and the scattering angle of D^{*-} from the associated events, the positions and the background shape in the missing mass

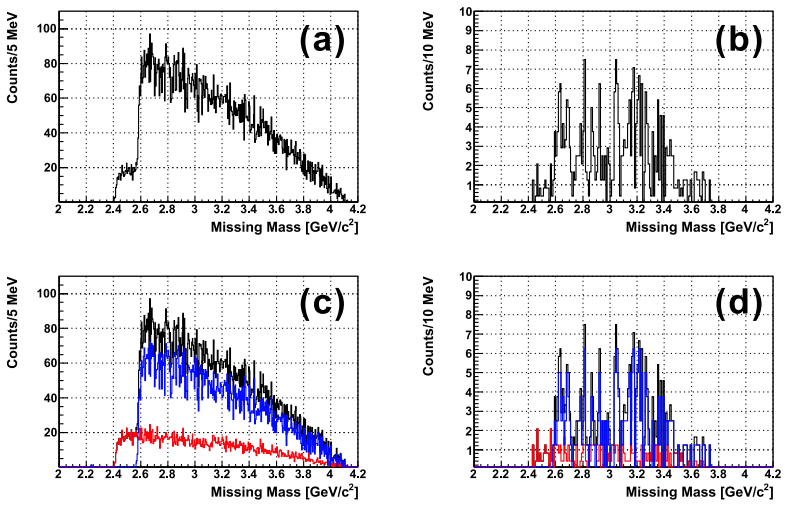

FIG. 20: The missing mass spectra of the non-resonant $D^{*-}+\pi$ production events. (a,c) and (b,d) show the spectrum with only the D^* tagging and both the D^* tagging and the event selections by using the kinematical conditions, respectively. The black liens show the sum spectra. The red and blue line show the missing mass spectra from $\Lambda_c^+ + D^{*-} + \pi^0$ and $\Sigma_c^{++,+,0} + D^{*-} + \pi^{-,0,+}$, respectively.

spectrum were also changed. Those possible peaking background sources can be identified.

Figure 23 show the missing mass spectrum of the sum of all channels. In the figure, 10 times larger number of events (corresponded to 10 nb/ch case) were generated. The D^{**} production was dominant background. This reaction makes a step structure in the background spectrum. The position of the step and the amount of the background events are related to the generated Y_c. The background shape and yield can be estimated from the Y_c spectrum.

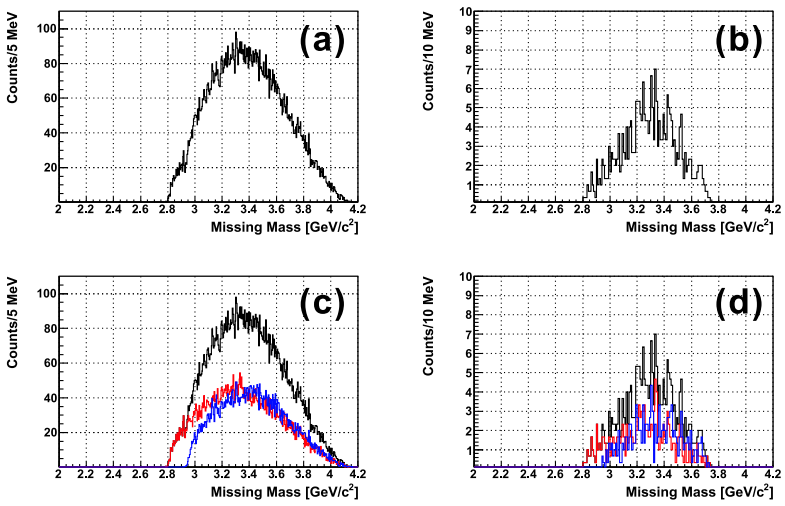

FIG. 21: The missing mass spectra of the non-resonant $D\bar{D}$ pair production events. (a,c) and (b,d) show the spectrum with only the D^* tagging and both the D^* tagging and the event selections by using the kinematical conditions, respectively. The black liens show the sum spectra. The red and blue line show the missing mass spectra from $D^{*+} + D^{*-} + n$, $D^{*0} + D^{*-} + p$ and $D^{+} + D^{*-} + n$ and $D^{0} + D^{*-} + p$, respectively.

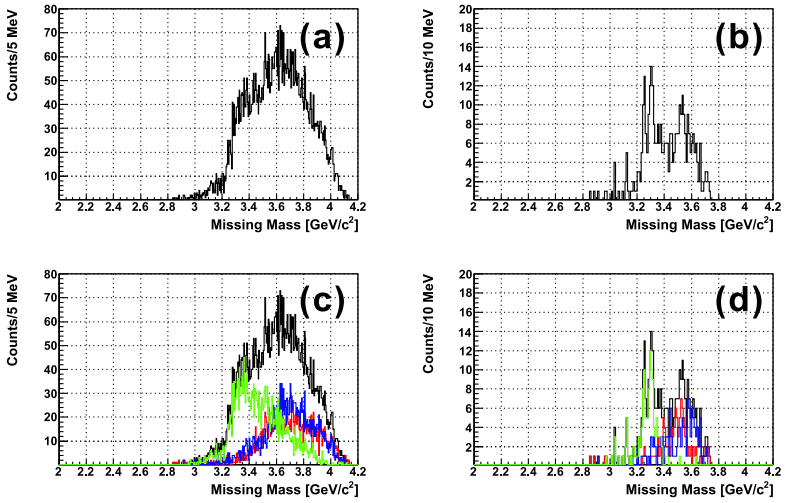

FIG. 22: The missing mass spectra of the $c\bar{c}$ meson production events. (a,c) and (b,d) show the spectrum with only the D^* tagging and both the D^* tagging and the event selections by using the kinematical conditions, respectively. The black liens show the sum spectra. The red, blue and green line show the missing mass spectra from the $\psi(4040)$, $\psi(4160)$ and $\psi(4415)$ production, respectively.

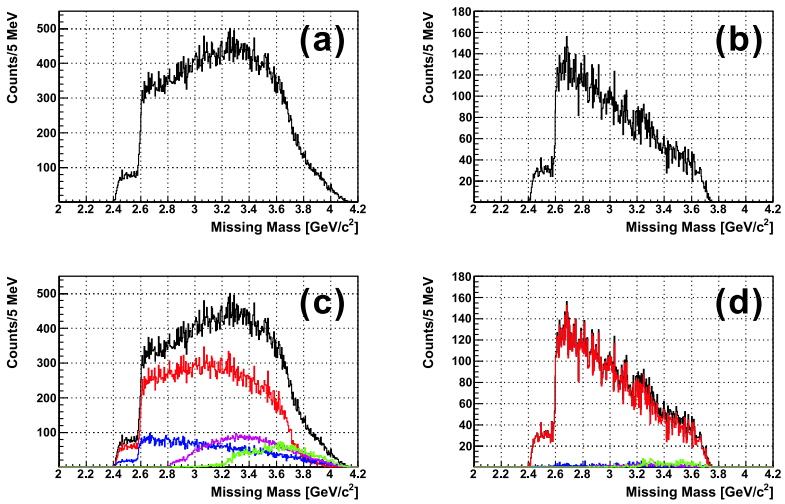

FIG. 23: The missing mass spectra of the sum of all channels. (a,c) and (b,d) show the spectrum with only the D^* tagging and both the D^* tagging and the event selections by using the kinematical conditions, respectively. The black liens show the sum spectra. The red, blue, green and purple line show the missing mass spectra of the D^{**} production, the non-resonant $D^{*-} + \pi$ production, the non-resonant $D\bar{D}$ pair production and the $c\bar{c}$ meson production, respectively.

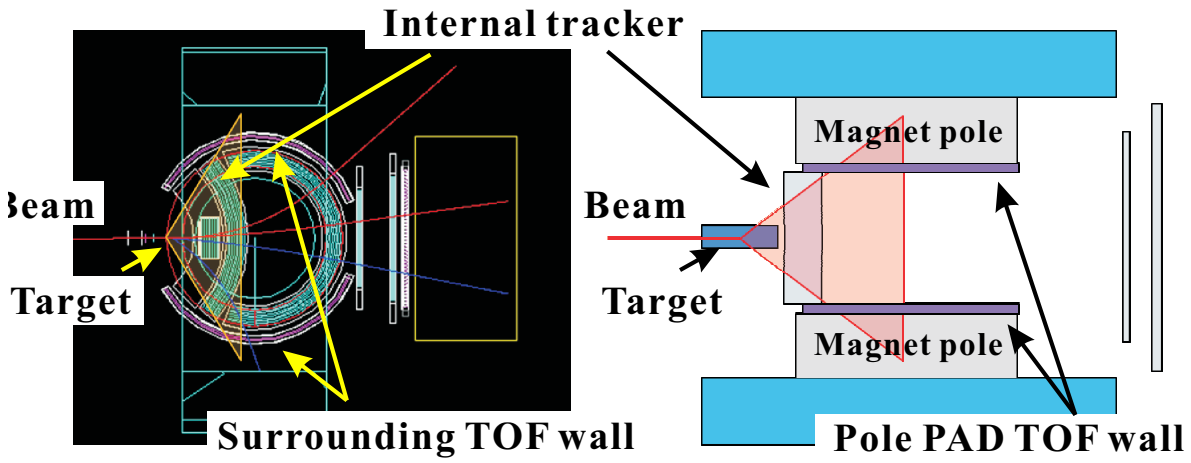

FIG. 24: The modified points of the spectrometer system. The surrounding TOF detectors and the pole pad-type detectors were installed around the magnet pole peace for horizontal measurement and on the face of the magnet pole for vertical measurement, respectively.

Appendix E: Performances of the spectrometer

In the experiment, the $\pi^- + p \rightarrow Y_c^{*+} + D^{*-}$ reaction is used. The D^{*-} meson decays by the $D^{*-} \rightarrow \bar{D}^0 + \pi^-$ channel (branching ratio of 67.7%). Then, the $\bar{D}^0$ meson decays by the $\bar{D}^0 \rightarrow K^+ + \pi^-$ channel (branching ratio of 3.88%). The decay products of K^+ and π^- from $\bar{D}^0$ and π^- from D^{*-} are mainly detected by the spectrometer. The spectrometer is designed to detect the final state of the "K^+, π^-, π^-" mode. The other decay modes of the $\bar{D}^0$ meson which have all charged particles ($\bar{D}^0 \rightarrow K^+ + \pi^- + \pi^+ + \pi^-$) can be also measured. In addition, the decay analysis can be performed by detecting decay products from the produced $Y*+_c$, such as as the $Y_c^{*+} \rightarrow \Sigma_c(2455)^{++,0} + \pi^{-,+}$, $Y_c^{*+} \rightarrow \Lambda_c^+ + \pi^+ + \pi^-$ and $Y_c^{*+} \rightarrow p + D^0$ channels. The recoil momentum of Y_c^{*+} is measured by the missing mass method so that the mass of the decay products ($\Sigma_c(2455)^{++,0}$ and D^0) can be extra-tagged by only detecting the emitted pions and protons.

For detecting the decay products from Y_c^{*+}, the surrounding TOF detectors and the pole pad-type detectors were installed around the magnet pole peace for horizontal measurement and on the face of the magnet pole for vertical measurement, respectively. In addition, the tracking detectors which have the larger angular acceptance were installed at the downstream of the target. Figure 24 shows the modified points of the spectrometer system. By using the those TOF walls and the tracking detectors, both the polar and azimuthal angle can completely be measured with more than $\cos\theta_{CM} = -0.5$ for the $\Lambda_c(2940)^+ \rightarrow \Sigma_c(2455)^{++,0} + \pi^{-,+}$ decay mode.

The acceptances for the detection of the D^{*-} decay are ~60% and ~50% for the 2-body and 4-body decay mode, respectivly as shown in Fig. 25. From the production cross section

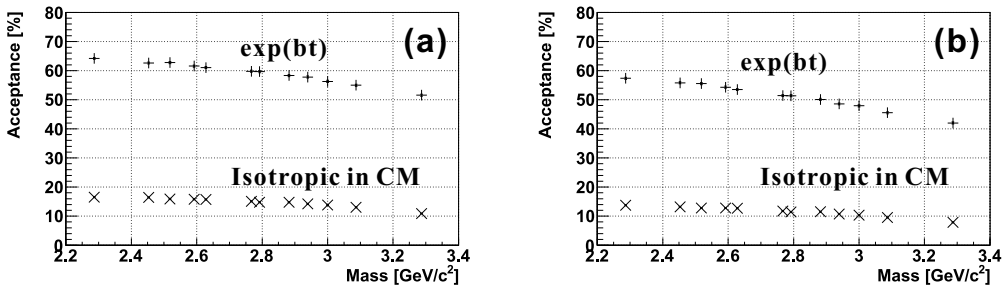

FIG. 25: Acceptance for D^{*-} as a function of the missing baryon mass for the 2-body(a) and 4-body(b) decay mode. The D^{*-} meson was generated with the $exp(bt)$ and isotropic distribution in the center-of-mass system, respectively.

studies, the t-channel process is considered to be dominant so that the angular distribution of $exp(bt)$ was used to estimate the acceptance. The yields is estimated to be ∼1900 and ∼3200 counts calculated by the experimental conditions for the 100-day beam time for the 2-body and 4-body decay mode, respectively.

The invariant mass resolution for reconstructing the $\bar{D}^0$ and D^{*-} are estimated to be 5.5 MeV and 0.7 MeV, respectively. The missing resolution by assuming the production of the ground state (Λ_c) and the excited state ($\Lambda_c(2880)^+$) are estimated to be 16 MeV and 9 MeV, respectively. The lower excited states can be separated from each other. The mass resolution higher than 2.8 GeV/c^2 was estimated to be several MeV. The resonances which have a decay width of more than several MeV can be measured.

The missing mass resolution turned to be worse due to the kinematic conditions by changing the beam momentum to be 20 GeV/c, while the momentum resolution (Δp/p∼0.2% at 5 GeV/c) was not changed by taken into account the position resolution of the tracking devices (0.1 mm for SSD, 0.2 mm for drift chambers and fiber trackers). The contribution of the momentum resolution of beam and scattered particles and the scattering angle term are balanced. In the kinematical condition of the $\Lambda_c(2880)^+$ production, the contributions of each term were ∼5 MeV, while the target energy loss straggling was ∼2 MeV. The resolution of ∼9 MeV can be estimated ($\Delta M^2 = 9^2 \sim 5^2 + 5^2 + 5^2 + 2^2$).

The mass resolution of the decay measurement is ∼10 MeV for the $\Lambda_c(2940)^+ \rightarrow \Sigma_c(2455)^{++,0} + \pi^{-,+}$ decay mode. The decay particles tracks were analyzed by only using the tracking detectors at the downstream of the target. The resolution is enough to separate the decay modes of $\Lambda_c(2940)^+ \rightarrow \Sigma_c(2455)^{++,0} + \pi^{-,+}$ and $\Lambda_c(2940)^+ \rightarrow \Sigma_c(2520)^{++,0} + \pi^{-,+}$.

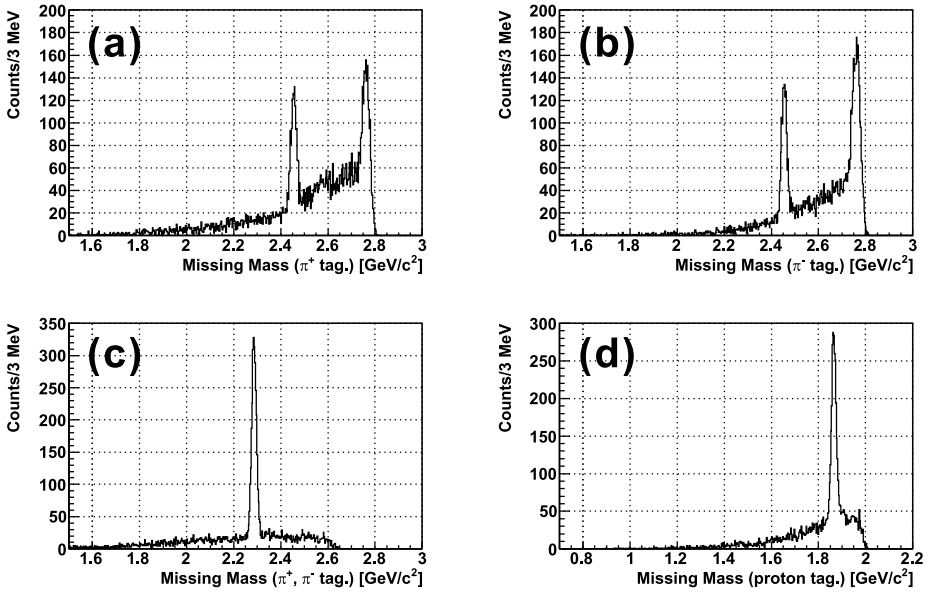

FIG. 26: The missing mass spectra by tagging the decay products from $\Lambda_c(2940)^+$ only including charmed baryon decay events. (a), (b), (c) and (d) show the decay mode of $\Sigma_c(2445)^0 + \pi^+$, $\Sigma_c(2445)^{++} + \pi^-$, $\Lambda_c^+ + \pi^+ + \pi^-$ and $p + D^0$, respectively.

Appendix F: Decay measurement

For the decay measurement, the event selection of the scattering angle selection of K^+ in the center-of-mass system was not applied because the signal acceptance become twice and the background level was decreased by selecting the decay products. The decay analysis can be performed by detecting decay products from the produced $Y*+_c$, such as as the $Y_c^{*+} \to \Sigma_c(2455)^{++,0} + \pi^{-,+}$, $Y_c^{*+} \to \Lambda_c^+ + \pi^+ + \pi^-$ and $Y_c^{*+} \to p + D^0$ channels. The recoil momentum of Y_c^{*+} is measured by the missing mass method so that the mass of the decay products ($\Sigma_c(2455)^{++,0}$ and D^0) can be obtained by only detecting the emitted pions and protons.

The missing mass spectra by tagging the decay products have clear peak as shown in Fig. 26. In this spectra, charmed baryon decay events are only included. The continuum background are made from the decay products from daughter particles such as Λ_c^+ and $\bar{D}^{+,0}$. In particular, the peak structure appear in the threshold region (M$\sim$2.75 GeV/c) in the $\pi^\pm$ tagging spectra. This peak structure is the combinatorial background by detecting the other π from the decay chain of $\Lambda_c(2940)^+ \to \Sigma_c(2445)^{++,0} + \pi^{-,+} \to \Lambda_c^+ + \pi^+ + \pi^-$. Those peaking background can be identified from the analysis by checking the correlation between the missing mass and the tagging missing mass.

Figure 27, Fig. 28, Fig. 29 and Fig. 30 show the the π^+, π^-, $\pi^+ + \pi^-$ and proton tagged missing mass spectra, respectively. In the figures, the switches of each decay mode are

only tuned on in the simulation. By tagging the decay products, the background shape from other channels were turned to be continuum. The continuum background are made from the decay products from daughter particles such as Λ_c^+ and $\bar{D}^{+,0}$. Only the $\Sigma_c(2455)^{++,0} + \pi^{-,+}$ modes have the peaking background around the threshold region (M$\sim$2.75 GeV/c). This peak structure is the combinatorial background by detecting the other π from the decay chain of $\Lambda_c(2940)^+ \to \Sigma_c(2445)^{++,0} + \pi^{-,+} \to \Lambda_c^+ + \pi^+ + \pi^-$.

The contribution from the wrong parties identification by the internal TOF wall and the pole pad-detector was estimated. The miss-PID of K^+ from π^+ is negligible because the Λ_c^+ branching ratio of emitting K^+ is very small. The protons are well separated from π^+ and K^+ and clearly identified by the detectors. If all the particles are not identified except its charge, the contribution of the miss-PID of K^- from π^- are almost the same as of π^- by considering the branching ratio of Λ_c^+. The background shape turn to be continuum and those events cannot make a pecking background in the tagging missing mass spectrum. Although the background level was twice larger in the case of the π^- tagging spectrum, the effect of the contribution from the wrong parties identification from the Λ_c^+ decay was small enough for the decay measurement.

For the strangeness production events, the contribution from the wrong parties identification by the internal TOF wall and the pole pad-detector was estimated. The miss-PID of K^+ from π^+ is negligible because the multi-K^+ production rate was $\sim$3% from JAM. The protons are separated well from π^+ and K^+ and clearly identified by the detectors. If all the particles are not identified except its charge, The miss-PID of K^- from π^- are $\sim$10% by considering the number of K^- which remain in the final events. The anti-protons are also separated well from π^- and K^- and clearly identified by the detectors. Those background shapes were continuum and those events cannot make a pecking background in the tagging missing mass spectrum. The effect of the contribution from the wrong parties identification from the strangeness production was estimated to be small.

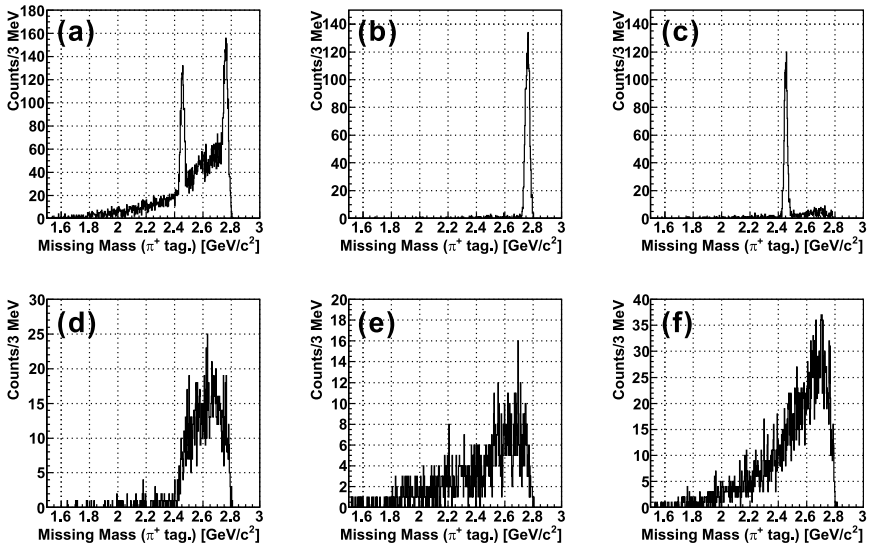

FIG. 27: The missing mass spectra by tagging π^+ from the $\Lambda_c(2940)^+$ decay. (a) show the inclusive spectrum. (b), (c), (d), (e) and (f) show the decay mode of $\Sigma_c(2445)^{++} + \pi^-$, $\Sigma_c(2445)^0 + \pi^+$, $\Lambda_c^+ + \pi^+ + \pi^-$, $p + D^0$ and other decay channels ($\Sigma_c(2445)^0 + \pi^0$, $\Lambda_c^+ + \pi^0 + \pi^0$, $n + D^+$), respectively.

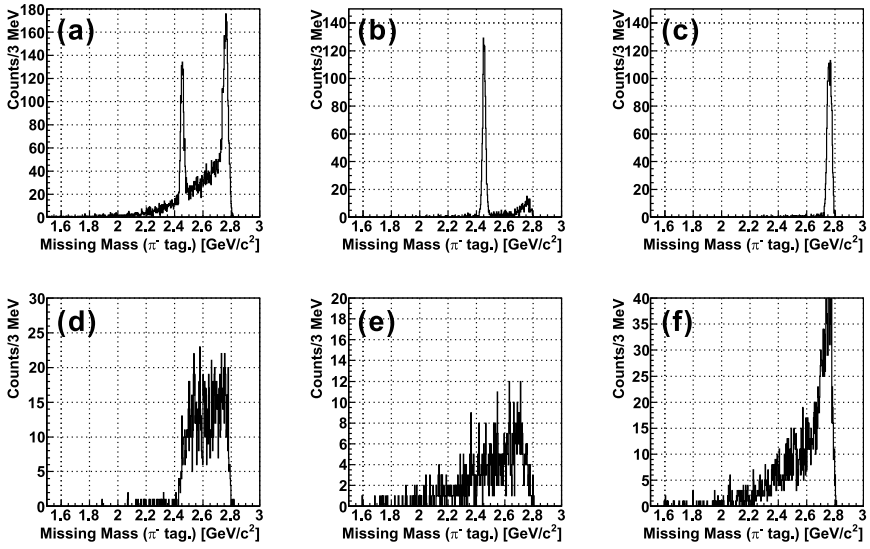

FIG. 28: The missing mass spectra by tagging π^- from the $\Lambda_c(2940)^+$ decay. (a) show the inclusive spectrum. (b), (c), (d), (e) and (f) show the decay mode of $\Sigma_c(2445)^{++} + \pi^-$, $\Sigma_c(2445)^0 + \pi^+$, $\Lambda_c^+ + \pi^+ + \pi^-$, $p + D^0$ and other decay channels ($\Sigma_c(2445)^0 + \pi^0$, $\Lambda_c^+ + \pi^0 + \pi^0$, $n + D^+$), respectively.

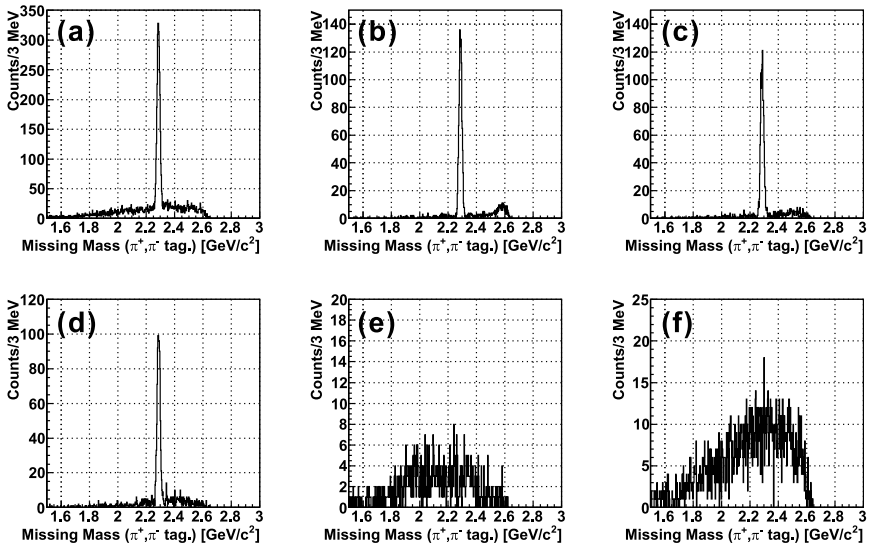

FIG. 29: The missing mass spectra by tagging $\pi^+ + \pi^-$ from the $\Lambda_c(2940)^+$ decay. (a) show the inclusive spectrum. (b), (c), (d), (e) and (f) show the decay mode of $\Sigma_c(2445)^{++} + \pi^-$, $\Sigma_c(2445)^0 + \pi^+$, $\Lambda_c^+ + \pi^+ + \pi^-$, $p + D^0$ and other decay channels ($\Sigma_c(2445)^0 + \pi^0$, $\Lambda_c^+ + \pi^0 + \pi^0$, $n + D^+$), respectively.

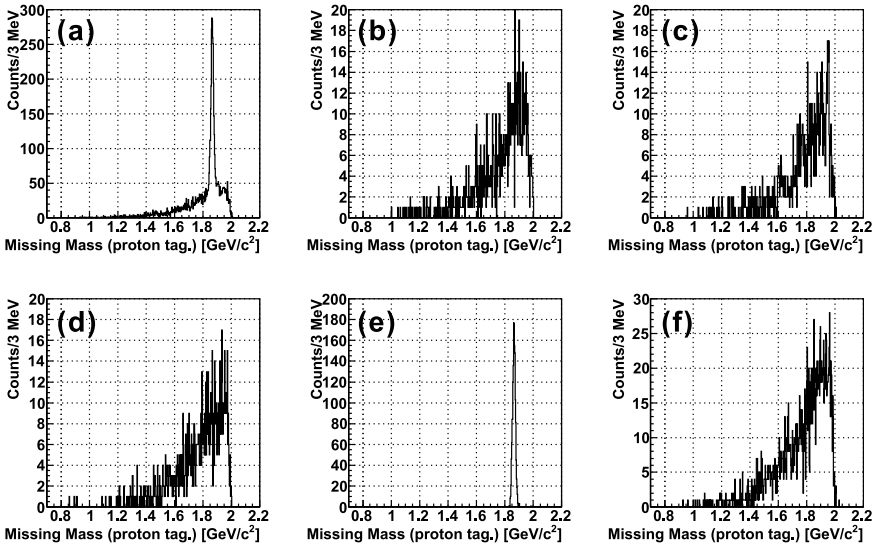

FIG. 30: The missing mass spectra by tagging proton from the $\Lambda_c(2940)^+$ decay. (a) show the inclusive spectrum. (b), (c), (d), (e) and (f) show the decay mode of $\Sigma_c(2445)^{++} + \pi^-$, $\Sigma_c(2445)^0 + \pi^+$, $\Lambda_c^+ + \pi^+ + \pi^-$, $p + D^0$ and other decay channels ($\Sigma_c(2445)^0 + \pi^0$, $\Lambda_c^+ + \pi^0 + \pi^0$, $n + D^+$), respectively.

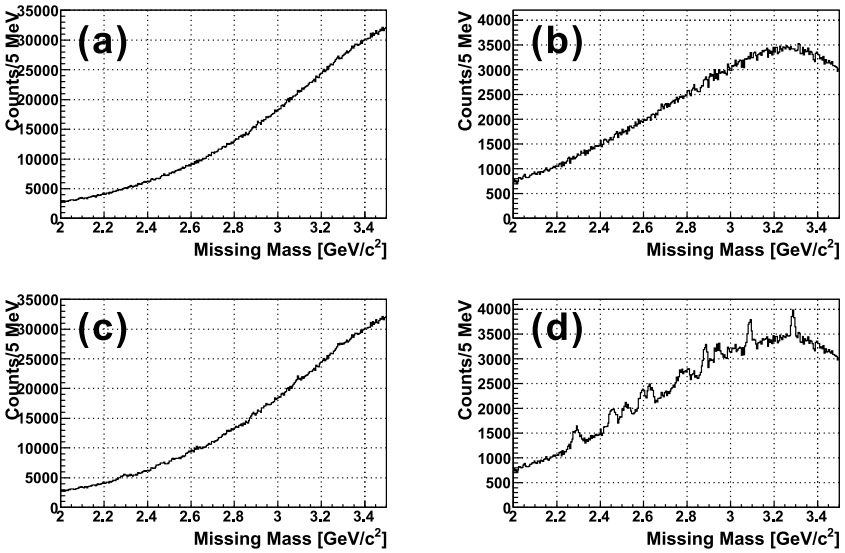

FIG. 31: The missing mass spectra of the 4-body $\bar{D}^0$ decay mode with the background reduced only by the D^* tagging (a,c) and by the the D^* tagging with the event selections (b,d). (a,b) shows the simulation results of the background events. (c,d) shows the spectra with the signal events.

1. Decay measurement with the $\bar{D}^0 \to K^+ + \pi^- + \pi^+ + \pi^-$ mode

To increase the number of decay events, the 4-body mode ($\bar{D}^0 \to K^+ + \pi^- + \pi^+ + \pi^-$) was analyzed. Figure 31 shows the missing mass spectra by analyzing the $\bar{D}^0 \to K^+ + \pi^- + \pi^+ + \pi^-$ decay mode. In the case of the 4-body mode, the background of the missing mass spectrum from the strangeness production turned to be much larger than that of the 2-body mode($\bar{D}^0 \to K^+ + \pi^-$), because the combination of events which can easily reconstruct the $\bar{D}^0$ mass are drastically increased. The missing mass including strangeness production background by tagging the decay particles has large background events as shown in Fig. 32.

By gating the Λ_c^+ mass region in the $\pi^+ + \pi^-$ tagging events, the background level was reduced as shown in Fig. 33. Due to the larger branching ration of the $\bar{D}^0 \to K^+ + \pi^- + \pi^+ + \pi^-$ mode (8.07%) than that of the $\bar{D}^0 \to K^+ + \pi^-$ mode (3.88%), the 2.5 times large number of events can be used for the decay measurement.

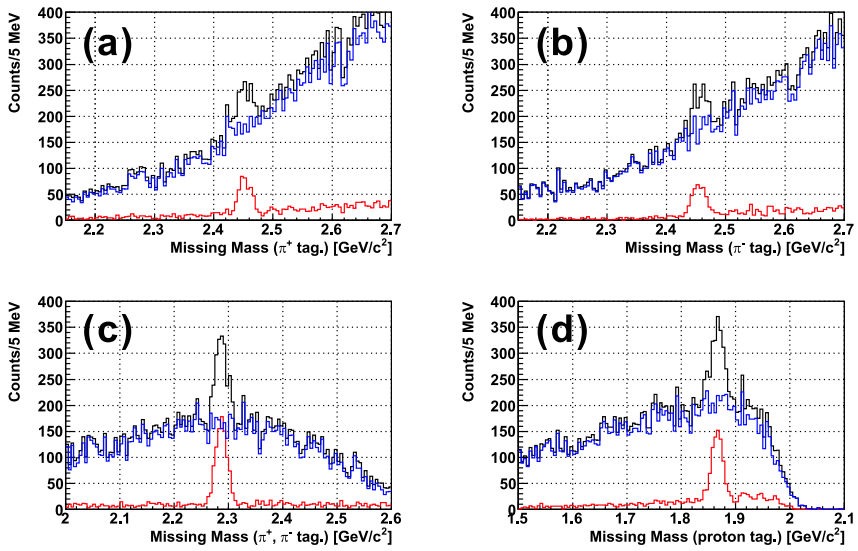

FIG. 32: The missing mass spectra by tagging the decay products from $\Lambda_c(2940)^+$ including the strangeness production background. (a), (b), (c) and (d) show the decay mode of $\Sigma_c(2445)^0 + \pi^+$, $\Sigma_c(2445)^{++} + \pi^-$, $\Lambda_c^+ + \pi^+ + \pi^-$ and $p + D^0$, respectively. The black, red, blue lines are the sum spectra, the charmed baryon decay events and the strangeness production background, respectively.

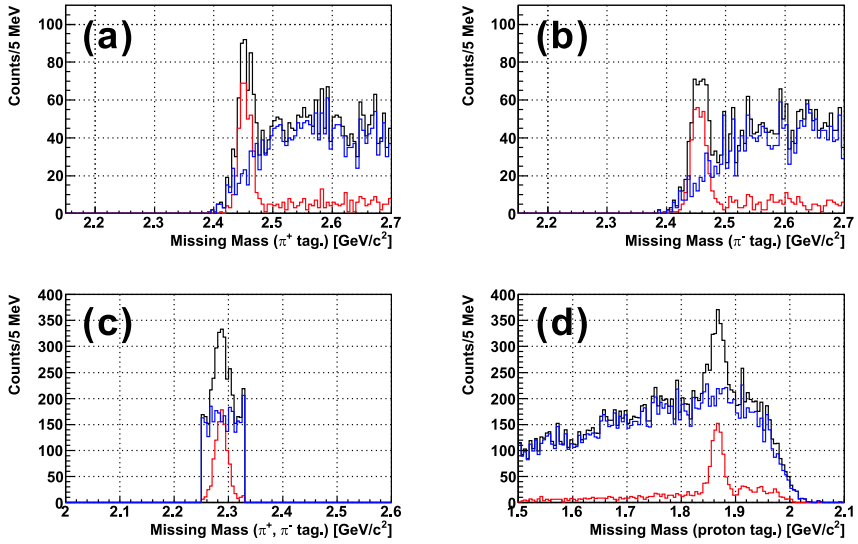

FIG. 33: The missing mass spectra by tagging the decay products from $\Lambda_c(2940)^+$ including the strangeness production background and by gating the Λ_c^+ mass region in the $\pi^\pm$ tagging events. (a), (b), (c) and (d) show the decay mode of $\Sigma_c(2445)^0 + \pi^+$, $\Sigma_c(2445)^{++} + \pi^-$, $\Lambda_c^+ + \pi^+ + \pi^-$ and $p + D^0$, respectively. The black, red, blue lines are the sum spectra, the charmed baryon decay events and the strangeness production background, respectively.

[1] Y. Nara *et al.*, Phys. Rev. C **61** 024901 (2000).

[2] T. Sjöstrand, S. Mrenna and P. Skands, JHEP05 (2006) 026, Comput. Phys. Comm. **178** (2008) 852.

[3] B. Andersson, G. Gustafson, G. Ingelman and T. Sjostrand, "Parton Fragmentation And String Dynamics", Phys. Rept. **97**, 31 (1983).

[4] J. H. Christenson *et al.*, Phys. Rev. Lett. **55**, 154 (1985).

[5] B. Ghidini *et al.*, Nucl. Phys. B **111**, 189 (1976).

[6] R. Honecker *et al.*, Nucl. Phys. B **13** 571 (1969).

[7] F. Barreiro *et al.*, Phys. Rev. D **17**, 669 (1978).

[8] D. J. Lange, "The EvtGen particle decay simulation package", Nucl. Instrum. Methods. A **462** 152 (2001).

[9] J. Beringer *et al.* (Particle Data Group), Phys. Rev. D **86**, 010001 (2012).